Icarus 207 (2010) 409–432

Contents lists available at ScienceDirect

Icarus

journal homepage: www.elsevier.com/locate/icarus

A comprehensive numerical simulation of Io's sublimation-driven atmosphere

Andrew C. Walker [a,*], Sergey L. Gratiy [c], David B. Goldstein [a], Chris H. Moore [a], Philip L. Varghese [a], Laurence M. Trafton [b], Deborah A. Levin [c], Bénédicte Stewart [a]

[a] Department of Aerospace Engineering, University of Texas, Austin, TX 78712, United States
[b] Department of Astronomy, University of Texas, Austin, TX 78712, United States
[c] Department of Aerospace Engineering, Pennsylvania State University, University Park, PA 16802, United States

ARTICLE INFO

Article history:
Received 2 July 2009
Revised 12 January 2010
Accepted 13 January 2010
Available online 22 January 2010

Keywords:
Io
Atmospheres, Dynamics
Atmospheres, Structure
Jupiter, Satellites
Satellites, Atmospheres

ABSTRACT

Io's sublimation-driven atmosphere is modeled using the direct simulation Monte Carlo (DSMC) method. These rarefied gas dynamics simulations improve upon earlier models by using a three-dimensional domain encompassing the entire planet computed in parallel. The effects of plasma heating, planetary rotation, inhomogeneous surface frost, molecular residence time of SO_2 on the exposed (non-volatile) rocky surface, and surface temperature distribution are investigated. Circumplanetary flow is predicted to develop from the warm dayside toward the cooler nightside. Io's rotation leads to a highly asymmetric frost surface temperature distribution (due to the frost's high thermal inertia) which results in circumplanetary flow that is not axi-symmetric about the subsolar point. The non-equilibrium thermal structure of the atmosphere, specifically vibrational and rotational temperatures, is also examined. Plasma heating is found to significantly inflate the atmosphere on both the dayside and nightside. The plasma energy flux causes high temperatures at high altitudes but plasma energy depletion through the dense gas column above the warmest frost permits gas temperatures cooler than the surface at low altitudes. A frost map (Douté, S., Schmitt, B., Lopes-Gautier, R., Carlson, R., Soderblom, L., Shirley, J., and the Galileo NIMS Team [2001]. Icarus 149, 107–132) is used to control the sublimated flux of SO_2 which can result in inhomogeneous column densities that vary by nearly a factor of four for the same surface temperature. A short residence time for SO_2 molecules on the "rock" component is found to smooth lateral atmospheric inhomogeneities caused by variations in the surface frost distribution, creating an atmosphere that looks nearly identical to one with uniform frost coverage. A longer residence time is found to agree better with mid-infrared observations (Spencer, J.R., Lellouch, E., Richter, M.J., López-Valverde, M.A., Jessup, K.L, Greathouse, T.K., Flaud, J. [2005]. Icarus 176, 283–304) and reproduce the observed anti-jovian/sub-jovian column density asymmetry. The computed peak dayside column density for Io assuming a surface frost temperature of 115 K agrees with those suggested by Lyman-α observations (Feaga, L.M., McGrath, M., Feldman, P.D. [2009]. Icarus 201, 570–584). On the other hand, the peak dayside column density at 120 K is a factor of five larger and is higher than the upper range of observations (Jessup, K.L., Spencer, J.R., Ballester, G.E., Howell, R.R., Roesler, F., Vigel, M., Yelle, R. [2004]. Icarus 169, 197–215; Spencer et al., 2005).

© 2010 Elsevier Inc. All rights reserved.

1. Introduction

In 1964, Binder and Cruikshank reported post-eclipse brightening when observing Io (Binder and Cruikshank, 1964) and attributed the anomalous brightening to a frost deposit or a haze layer caused by the surface temperature drop during eclipse. But the existence of an atmosphere remained in question due to the conflicting results of other observations in search of post-eclipse brightening (O'Leary and Veverka, 1971; Franz and Millis, 1971; Cruikshank and Murphy, 1973). In 1973, Pioneer 10 detected and probed Io's ionosphere through radio occultation providing proof of an atmosphere on Io. Kliore et al. (1975) modeled the Pioneer data to estimate a surface pressure between 1 and 10 nbar near the terminator. It was not until 1979 that the primary dayside species, sulfur dioxide, was detected by the Voyager IR spectrometer (IRIS) (Pearl et al., 1979). Lellouch et al. (1992) later reinterpreted the same IRIS data but included non-local thermodynamic equilibrium (non-LTE) effects to infer surface pressures in the 5–40 nbar range. The UV spectral observations of Ballester et al. (1990) are best fit by a cool gas with large spatial extent, supporting a sublimated atmosphere. However, millimeter-wave observations of the

* Corresponding author.
E-mail address: andrew.walker@mail.utexas.edu (A.C. Walker).

0019-1035/$ - see front matter © 2010 Elsevier Inc. All rights reserved.
doi:10.1016/j.icarus.2010.01.012

222 GHz rotational line of SO_2 (Lellouch et al., 1990) are best fit by a warm gas with limited extent and are argued to be best matched by volcanic models (Lellouch et al., 1992).

As illustrated by the conflicting observations of Ballester et al. (1990) and Lellouch et al. (1990), there are two important mechanisms on Io which could produce a substantial atmosphere: volcanic activity and sublimation from surface frost. No observations have shown conclusively which mechanism is the dominant producer of Io's atmosphere. Spencer et al. (2005) give a detailed review and discussion of the various observations supporting either volcanic or sublimated atmospheres. We simulate the sublimated flux of SO_2 from the surface frost and attempt to reconcile the resulting atmosphere with observations. In cases where the sublimation atmosphere does not agree with the observations, we have superimposed 10 "persistent" volcanic plumes (Geissler et al., 2004) which are believed to have been active during the IR observations of Spencer et al. (2005) to determine if a combination of volcanic and sublimated support provides better agreement with the observations. The plumes (Pele, Kanehikili, Masubi, Amirani, Thor, Prometheus, Culann, Zamama, Marduk, and Loki) are obtained from separate simulations. Our atmospheric model will be constrained by the more recent observations of the SO_2 column density on Io.

The local dayside SO_2 vertical column abundance varies between $\sim 5 \times 10^{15}\,cm^{-2}$ and $6 \times 10^{17}\,cm^{-2}$. These variations are likely due to actual variations in the column density due to the insolation, surface frosts, volcanoes, and lava lakes as well as the different measurement techniques and data analysis methods used. Estimates of the dayside vertical column densities fall into two categories: spatially unresolved, disk-integrated values and spatially resolved values.

UV Hubble Space Telescope (HST) disk-integrated observations made in 1992 utilizing the Faint Object Spectrograph (FOS) predict column densities of $6–10 \times 10^{15}\,cm^{-2}$ (Ballester et al., 1994) and $4 \times 10^{16}\,cm^{-2}$ (Clarke et al., 1994) for uniform atmospheric distributions. Ballester et al. (1994) also fit their spectra to localized atmospheric models with column densities of $10^{16}–3 \times 10^{17}\,cm^{-2}$. Jessup et al. (2002) analyzed additional HST/FOS observations made in 1994 and 1996 and fit the data with a two component model: an extended component at 110–350 K with column densities of $10^{15}–10^{16}\,cm^{-2}$ and a confined component at 105–115 K with column densities of $\sim 2.0 \times 10^{16}–2.0 \times 10^{17}\,cm^{-2}$. Trafton et al. (1996) inferred disk-averaged column densities of $5.0 \times 10^{15}\,cm^{-2}$ and $7.0 \times 10^{15}\,cm^{-2}$ for the leading and trailing hemispheres, respectively, from UV spectra observed with the Goddard High Resolution Spectrograph (GHRS) on HST. Disk-averaged observations at millimeter wavelengths (Lellouch et al., 1992) made with the IRAM (Institut de Radio-Astronomie Millimétrique) radiotelescope are best fit by local column densities of $\sim 10^{17}\,cm^{-2}$ and temperatures >600 K. Spencer et al. (2005) obtained disk-integrated mid-infrared spectra at the NASA Infrared Telescope which yielded inferred equatorial column densities of $1.5 \times 10^{17}\,cm^{-2}$ near 180°W and $1.5 \times 10^{16}\,cm^{-2}$ near 300°W. These results are discussed in detail in Section 2 as a key constraining observation.

More recently, observations that spatially resolve Io have been performed. The first successful spatially resolved observation of Io's atmosphere was performed in 1996 (McGrath et al., 2000) with HST/FOS. The UV observations reported spatial inhomogeneity in column densities between three separate locations: the Pele volcano, the Ra volcano, and a control region centered at 45°S and 300°W. The column densities at these locations were inferred to be $3.25 \times 10^{16}\,cm^{-2}$, $1.5 \times 10^{16}\,cm^{-2}$, and $7 \times 10^{15}\,cm^{-2}$, respectively. A 1998 observation made by the Galileo Ultraviolet Spectrometer with marginal disk resolution, and spectral resolution inadequate to resolve the 10 Å wide SO_2 absorption bands, yielded an inferred SO_2 abundance near $4 \times 10^{17}\,cm^{-2}$ covering ~25% of the observed region and a local abundance as high as $1 \times 10^{19}\,cm^{-2}$ (Hendrix et al., 1999). However, these high values are uncertain because they depend on assumptions about the reflectivity of Io's surface materials. HST observations utilizing the Space Telescope Imaging Spectrograph (STIS) in the Lyman-α (Roesler et al., 1999; Feldman et al., 2000) yield column densities of $\sim 10^{16}\,cm^{-2}$. Feaga et al. (2009) further analyzed the HST/STIS images; their results are discussed in detail in Section 2 as a key constraining observation for our atmospheric model.

Jessup et al. (2004) used HST/STIS mid- to near-UV observations to obtain spatially resolved column densities that generally vary between 10^{16} and $10^{17}\,cm^{-2}$ and peak near the equator at $1.25 \times 10^{17}\,cm^{-2}$ with an additional $5 \times 10^{16}\,cm^{-2}$ column near Prometheus. These inferred column densities are consistent with vapor pressure equilibrium (with a peak temperature of ~117 K) for latitudes <30° or solar zenith angles <40°. Beyond these latitudes and solar zenith angles, the inferred atmospheric column densities do not follow vapor pressure equilibrium. Jessup et al. give several explanations for the divergence from vapor pressure equilibrium: enhancement by dynamical flow, warm areas that inhibit condensation, and/or SO_2 plumes. Moullet et al. (2008) obtained the first disk-resolved millimeter observations using the IRAM Plateau de Bure Interferometer and inferred that the atmosphere covers ~80% of the leading side and ~60% of the trailing side. They also found a limb-to-limb velocity difference of 330 ± 100 m/s which is at odds with the models of Ingersoll et al. (1985), Ingersoll (1989) that predict uniform flow away from the subsolar point for uniform frost coverage. Moullet et al. hypothesize that the limb-to-limb velocity difference could be due to a plume near the limb or geographical variations in the surface pressure due to either thermal inertia or surface frosts.

The SO_2 surface frost abundance has been mapped by McEwen et al. (1988) based on Voyager multispectral mosaics, Carlson et al. (1997) with the Galileo near-infrared mapping spectrometer (NIMS) data, Douté et al. (2001) with hyperspectral data cubes from Galileo NIMS, and others (Nash et al., 1980; Nelson et al., 1980; Howell et al., 1984; Sartoretti et al., 1994; Geissler et al., 1999). McEwen et al. (1988) found that SO_2 frost is concentrated near the equator and is relatively deficient near Pele-type volcanoes and near the polar regions in stark contrast to the results of Douté et al. (2001). Carlson et al. (1997) found frost nearly everywhere with localized concentrations of thicker deposits the inferred locations of which vary with observation wavelength. At 3.35 μm, the frost abundance appears largely equatorial; however, there are polar deposits seen at both 2.79 μm and 3.78 μm.

More recently, Laver and de Pater (2008, 2009) have mapped the equivalent widths of two SO_2 frost absorption bands at 1.98 and 2.13 μm using the OH Suppressing Infra-Red Integral field Spectrometer (OSIRIS) on the W.M. Keck II telescope. In their 2008 paper, they found that the frost abundance (based on the equivalent widths) correlated more closely with the maps of McEwen et al. (1988) than those of Douté et al. (2001). They tentatively proposed that the differences between the maps may be due to the mapping of different grain sizes. In Laver and de Pater's most recent work (2009), they expanded upon their previous work by mapping both the trailing and leading hemispheres in the same two SO_2 frost absorption bands and by converting their equivalent widths into SO_2 frost abundance. The increased coverage allowed additional comparison to the SO_2 frost maps of Carlson et al. (1997). The Laver and de Pater (2009) frost maps are very similar to those of McEwen et al. (1988) and two of the Carlson et al. (1997) maps (derived from 2.79 μm to 3.35 μm bands of SO_2) all of which found large regions of SO_2 frost near the equator; however, they disagree with a third Carlson et al. (1997) frost map (derived from the 3.77 μm band of SO_2) and the frost map created by Douté et al. (2001). Laver and de Pater (2009) again theorize that

the disparity in the frost maps is due to the different grain sizes that are probed with the different spectral bands. They suggest that the weak SO_2 frost absorption bands (1.98 μm and 2.12 μm) are more sensitive to the older frost regions with larger grain sizes due to grain growth over time and are not able to probe the fine grains that may exist at higher latitudes. Douté et al. (2001) used a broad spectral region to map the SO_2 frosts and therefore were able to detect the fine grained frosts at higher latitudes. We have chosen to use the Douté et al. (2001) data in our simulations because they provide the most comprehensive map of Io's SO_2 frost distribution and appear to include the fine-grain polar deposits.

Spatially resolved observations have still not uncovered the dominant atmosphere production mechanism on Io. Our atmospheric model will attempt to answer this unresolved question. There have been several attempts to model Io's rarefied atmosphere, starting with Ingersoll et al. (1985). Ingersoll et al. vertically integrated the conservation equations and argued for the existence of sublimation-driven flow. They assumed turbulent atmospheric flow, a negligible effect from planetary rotation, and uniform frost coverage controlled by a surface in instantaneous radiative equilibrium with solar radiation. They found that pressure-driven supersonic flow develops as gas sublimates from areas near the warm subsolar region and condenses in the colder regions near the terminator. Similar results were found by Moreno et al. (1991) who allowed the atmosphere to vary with altitude and also included a crude radiative transfer model to account for atmospheric cooling to space and atmospheric heating from the surface. Both found that the net sublimation region extends from the subsolar point to a solar incidence angle $\theta \leq 37°$ with their particular assumptions. The net condensation region, where the atmospheric pressure becomes higher than the vapor pressure of SO_2, was found to occur beyond about 37°. Strobel et al. (1994) were the first to report on the importance of plasma heating on the vertical structure of Io's atmosphere. They developed a radiation–conduction model including the effects of solar, Joule, and plasma heating and found that the upper atmosphere is heated predominantly by Joule and plasma heating. Wong and Johnson (1995) computed the effect of plasma heating on Io's sublimation atmosphere and found it to significantly inflate the upper atmosphere. In 1996, Wong and Johnson (1996) improved upon their previous model by including photochemistry and tracking the daughter species of SO_2. More recently, Wong and Smyth (2000) refined the plasma model to allow incoming plasma ions to reaccelerate after a collision with a neutral in the atmosphere. Their result, which was qualitatively consistent with results of other models, showed that SO_2 was the dominant atmospheric species (compared to SO, S, O, O_2, and ions) and that the SO_2 column density dropped significantly on the nightside. Their ratio for the SO_2 density at the subsolar point to that of the nightside was $\sim 10^3$ and they suggested that other condensable species (S and O) follow this trend. In 2004, Smyth and Wong (2004) incorporated electron chemistry into their atmospheric model and found that the number densities of O, SO, S, and O_2 were greatly enhanced nearly everywhere and became comparable to SO_2 at high altitudes and on the nightside. These simulations all modeled the atmosphere as a continuum; this is a poor approximation at high altitudes and away from the subsolar region (see Fig. 3 in Austin and Goldstein (2000)).

Other simulations (Veeder et al., 1994; Kerton et al., 1996) have attempted to model the temperature distribution of Io's surface without computing the dynamics of its atmosphere. Such models are important as boundary conditions to our simulations. Veeder et al. (1994) compiled infrared radiometry data from between 1983 and 1993. They found that the data were best matched by a three component model composed of: (1) an equilibrium thermal unit (with zero thermal inertia so that it is in instantaneous radiative equilibrium), (2) a thermal reservoir unit (with infinite thermal inertia so that the temperatures are only a function of latitude), and (3) a thermal anomaly unit (hot spots). Kerton et al. (1996) modeled Io's temperature distribution while including the effects of latent heat of SO_2 frost sublimation/condensation, the rotation of Io, thermal conduction, internal heat flow, and the solid state greenhouse effect. They find that the surface temperatures are decreased by each effect except for the internal heat flow (which they assumed to be zero for most of their computations). Thermal inertia was found to have the largest effect (~14 K) when the thermal conductivity was close to the value of other planetary regolith materials. The latent heat caused a temperature drop of ~5 K and the solid state greenhouse effect dropped the temperature another ~2 K.

Several simulations have been performed using particle methods which can accurately model Io's rarefied atmosphere. Pospieszalska and Johnson (1996) used Monte Carlo calculations to characterize the effect of ion bombardment on the vertical structure and loss rate of Io's atmosphere. They found that the energy removed from the atmosphere by sputtering becomes a significant fraction of the plasma energy deposited for large ion cross sections and that this affects the exobase temperature, but leaves the exobase altitude and density virtually unchanged. Austin and Goldstein (2000) used the DSMC method to simulate the circumplanetary flow on Io. They presented a two-dimensional axi-symmetric simulation of sublimation/condensation driven flow and suggested that the atmospheric flow never reaches much past the terminator due to rapid condensation beyond the terminator shock or due to obstruction by non-condensable gases. Recently, Moore et al. (2009) used DSMC to simulate Io's sublimation atmospheric vertical dynamics throughout eclipse in the presence of non-condensable species (such as O_2 or SO). They found that, as the surface cooled, even moderate non-condensable mole fractions significantly slowed the condensation of the SO_2 atmosphere onto the surface as it cooled because of the formation of a thick diffusion layer of non-condensable gas near the surface.

Here we present the first global three-dimensional rarefied atmospheric model of Io's atmosphere which investigates the effects of surface temperature, planetary rotation, surface frosts, plasma heating, and residence time on a rock surface on Io's atmosphere. We analyze the resulting flows, column densities, and temperatures in an attempt to reconcile observations of the surface temperature distribution (Rathbun et al., 2004), surface frost abundance (Douté et al., 2001), column density (Feaga et al., 2009), and disk-averaged band depth of the ν_2 vibrational band of SO_2 (Spencer et al., 2005).

2. Constraining observations

In the last few years there have been many important observations which could help develop an understanding of the underlying physics that drive Io's complex atmosphere. As discussed later, we have attempted to reconcile various observations using our atmospheric model. These observations include Lyman-α radiation images which were used to map the dayside column densities on Io (Feaga et al., 2009), disk-integrated observations of the 19.3 μm SO_2 band (Spencer et al., 2005), surface temperature data from the Galileo photopolarimeter–radiometer (PPR) (Rathbun et al., 2004), and Galileo NIMS data which were used to derive the fractional abundance of SO_2 surface frost (Douté et al., 2001). The following section gives a brief summary of each data set.

Feaga et al. (2009) obtained Lyman-α spectroscopic data with HST. At 1216 Å, SO_2 is a continuum absorber with a large absorption cross-section, meaning that solar Lyman-α radiation will be attenuated by Io's column of SO_2. The attenuation enables for the derivation of the SO_2 atmosphere's spatial extent and column den-

sity. These derived vertical column densities were found to have small absolute temporal variation, except in specific locations usually around known volcanic centers. Feaga et al. (2009) also created a spatially smoothed global map of the SO_2 distribution from the individual images across all observed orbital longitudes by averaging the vertical column density at points where the images overlapped. The global map shows a distinct asymmetry between the abundance of SO_2 on the sub-jovian and anti-jovian hemispheres. The peak vertical column density was determined to be $5.0 \times 10^{16}\,cm^{-2}$ on the anti-jovian hemisphere, $4.2 \times 10^{16}\,cm^{-2}$ at the anti-jovian point, and $1.5 \times 10^{16}\,cm^{-2}$ at the sub-jovian point. The column densities at high latitudes above 45° were suggested to be below $1 \times 10^{14}\,cm^{-2}$. The anti-jovian hemisphere's peak vertical column density does not lie at the anti-jovian point possibly due to volcanic activity since the peak occurs (at 140°W along the equator) near Prometheus.

Spencer et al. (2005) obtained disk-averaged data from emission in the SO_2 ν_2 vibrational band at 19.3 μm at the NASA Infrared Telescope Facility on Mauna Kea in November 2001, December 2002, and January 2004. They modeled the vertical thermal structure of the atmosphere with the most important production and loss processes assuming non-LTE by simultaneously solving the statistical equilibrium equation of state and the radiative transfer equation. Their surface temperature model was compared to data from the Galileo PPR (Rathbun et al., 2004) and empirically weighted to increase the temperature near the subsolar point and decrease the temperature near the limb. Spencer et al. (2005) found that there are ambiguities in interpreting the IR spectra because an increase in density can lead to both higher and lower absorption strength depending on the vertical thermal structure present in the model atmosphere. An atmosphere with a modified latitudinal dependence (i.e. hydrostatic column densities everywhere except between absolute latitudes of 32° and 50°, where the column density is held fixed at the 32° latitude value) was found to be the best fit to the observations; however, it is only an empirical model and gives little insight into the physics which underlie the structure of the atmosphere. As discussed earlier, the inferred column densities were $1.5 \times 10^{17}\,cm^{-2}$ near 180°W and $1.5 \times 10^{16}\,cm^{-2}$ near 300°W.

Our modeled diurnal surface temperature variation is compared to data recorded by the Galileo spacecraft's PPR and NIMS instruments (Rathbun et al., 2004). The NIMS instrument measured emission from hot spots with temperatures greater than 200 K, while the PPR was able to probe the cooler temperatures of the passive background. The present simulations are compared to the temperatures derived from the PPR data because no hot spots are included in the model presented herein. Hot spots are excluded because they cover less than 1% of the surface area of Io (Sinton et al., 1980; Marchis et al., 2005). The PPR data were obtained using several filters from which a brightness temperature distribution was derived. At 27 μm, the dayside brightness temperature distribution showed the expected pattern with the temperature peaking near the subsolar point. Non-volcanic anomalies were present in the temperature distribution which could be attributed to variations in the thermal inertia of the surface. On the nightside, the brightness temperature is dominated by the presence of hot spots. The passive background nightside temperature was ~95 K both near the poles and equator, suggesting little drop-off with latitude. The brightness temperature presented by Rathbun et al. (2004) is a superposition of the radiation from hot spots, warm non-frost covered surfaces, and SO_2 frost covered surfaces. Rather than match the magnitude of the brightness temperature, which peaks at ~130 K (and most likely overestimates the actual frost temperature due to the averaging of the flux from frost covered areas with the flux from hot spots and warm non-frost covered areas), we have attempted to match the nightside cooling rate of the brightness temperature seen in the Galileo PPR observations (Rathbun et al., 2004).

The distribution of SO_2 frost on Io's surface should be closely linked with the surface temperature and the column density if the atmosphere is driven by sublimation. Douté et al. (2001) investigated the abundance of SO_2 frost by analyzing images acquired by the Galileo NIMS instrument. By assuming that the deposits of SO_2 frost are optically thick and geographically mixed, they found the SO_2 frost distribution over about three quarters of Io's surface (while the remaining quarter of the surface was not observed). They found that frost is omnipresent over Io's surface but is concentrated within several large areas centered at medium latitudes which show a longitudinal correlation with the distribution of plumes at lower latitudes (Douté et al., 2001). Although there are no data from 0°W to approximately 60°W longitude, the sub-jovian longitudes between 270°W and 360°W show a lower average frost abundance than the anti-jovian hemisphere, which could relate to the anti-jovian hemisphere having a higher atmospheric vertical column density.

3. Model

Here we present a fully three-dimensional model of Io's sublimation atmosphere computed using the DSMC method (Bird, 1994). The atmospheric density is controlled by the local vapor pressure and local areal coverage of SO_2 surface frost. The gas densities span the range from highly collisional (near the peak surface frost temperature at low altitudes) to free molecular flow (at high altitudes and on the nightside). Previous models of Io's atmosphere have been either one-dimensional, in which only the vertical structure and temporal evolution are investigated, or two-dimensional, which are axi-symmetric about the subsolar point. Also, some previous computational models approximated Io's rarefied atmosphere as a continuum, whereas our model uses the DSMC method which is valid throughout the entire atmosphere. Our three-dimensional simulation is able to model asymmetries in atmospheric parameters such as density, temperature, and flow velocity due to planetary rotation and an inhomogeneous frost distribution. We simulate only the dominant dayside species, SO_2, as previous observations (Lellouch, 1996a,b; Feaga, 2005) have found that on the dayside the concentrations of SO_2 daughter species are generally less than 10%. We realize that the daughter species can be important as non-condensables; however, from a computational standpoint, modeling the trace species on Io is costly in 3D and has not been included in the current work. Our global gas dynamic model is compared to observations in the mid-infrared (Spencer et al., 2005), Lyman-α (Feaga et al., 2009), and millimeter ranges (Moullet et al., 2008) by using a backwards Monte Carlo radiative transfer code (Gratiy et al., 2009) whose results are presented in a companion paper.

3.1. DSMC method

The range of flow densities on Io fluctuates greatly from $\sim 10^{11}\,cm^{-3}$ at low altitudes near the peak surface frost temperature to fewer than $10^3\,cm^{-3}$ at high altitudes on the nightside. The atmosphere on and near the nightside is of such low density that the mean free path exceeds the length scales associated with gradients in the gas properties. Continuum models break down when the characteristic length scale of the flow becomes comparable to the mean free path of the flow, so a rarefied gas dynamic technique must be applied. In such rarefied flow conditions, the DSMC method (Bird, 1994) is the most suitable choice. DSMC is advantageous because it is physically accurate in all flow regimes, although it becomes computationally expensive at high densities.

In the DSMC method, the flow is modeled by computational molecules (representing a far greater number of real molecules) that move and collide. Atmospheric properties in a cell, such as temperature and density, are extracted by sampling and averaging over all of the computational molecules within the cell. The collision model used is the variable hard sphere (VHS) model, with the appropriate parameters for SO_2 molecules (Bird, 1994).

Our current DSMC code includes many adaptations and modifications of Bird's original DSMC procedure (Zhang et al., 2003; Stewart et al., 2009). The molecules experience a gravitational body force and therefore travel along ballistic trajectories after sublimating from the surface. The rotational and vibrational energy states of SO_2 molecules are tracked and internal energy exchange occurs during collisions. Rotational energy levels are considered to be continuous while vibrational energy states are discrete due to the relatively cold temperatures in Io's atmosphere; all three modes of vibration are treated for SO_2. The vibrational and rotational states are initially populated at the inner boundary (the surface of Io) by assuming that sublimated molecules are in thermal equilibrium with the surface. During the gas dynamics calculation, the atmosphere is assumed to be optically thin, so that any radiation emitted from an SO_2 molecule is lost to space or Io's surface. For a detailed account of the internal energy exchange and radiation modeling, see Zhang et al. (2003). Plasma bombardment by ions, neutrals, and electrons from Jupiter's co-rotating plasma torus is modeled via a plasma energy flux. The implementation of the plasma heating model is discussed in more detail in Section 3.8. The surface frost coverage is modeled using derived frost fractions from hyperspectral images acquired by Galileo's NIMS (Douté et al., 2001). The implementation of the surface frost model is discussed in detail in Section 3.3. The planetary rotation of Io is included through the spatially and temporally varying temperature distribution model but the Coriolis force is neglected.

3.2. 3D geometry and parallelization

The computational model uses a three-dimensional spherical geometry with the domain spanning all latitudes and longitudes and from Io's surface to 200 km altitude. In our coordinate system, west is the direction of increasing longitude. The upper edge of the domain has a vacuum boundary condition such that all molecules crossing that boundary are deleted. This boundary condition for the upper edge is acceptable because the number densities at that altitude are very low ($\sim 10^{-3}$ of the gas number density near the surface) and there is little gas escaping that does not have escape velocity. Any error that this causes will be confined to minor changes in the radial velocity. The lower edge of the domain is the surface, which is defined to have a unit sticking coefficient based on our sublimation model (Wagman, 1979; Zhang et al., 2003). Molecules which strike the surface have a probability of striking either frost or a non-volatile (rock) depending on the frost fraction for that surface cell. The grid is stretched exponentially in the radial direction to keep the cell height equal to or less than the local mean free path $\lambda = 1/(\sqrt{2}\pi n d)^2$, where $d = 7.16 \times 10^{-10}$ m is the effective diameter of SO_2. For a surface temperature of 120 K, the mean free path directly above the surface is ~1.5 m, but the mean free path grows exponentially with altitude and with solar zenith angle. At a lower surface temperature of 115 K, the local mean free path is ~7.5 m. The grid stretching rate is dependent only on the local surface temperature which results in a different grid stretching across processors. The cell size at high altitudes is limited to 5 km so as to remain smaller than the scale height of the atmosphere. The scale height, H, is approximately 8.3 km at the surface; where $H = RT/g$, R is the gas constant, T is the gas temperature, and g is the gravitational acceleration on Io. The grid size exceeds the mean free path in longitude and latitude, but grid convergence studies were performed showing that the length scale of gradients in these directions remains satisfactorily greater than the cell size.

The cell sizes in latitude and longitude have a resolution of 1°, giving 180 cells in the polar direction and 360 cells in the azimuthal direction. The large numbers of computational cells and simulated particles require the use of parallel computers (Stewart et al., 2009). The domain is decomposed in the azimuthal direction between 360 processors (for 180°W subsolar longitude case), with each processor receiving 1° of longitude, see Fig. 1. All other subsolar longitudes are computed with 36 processors; the remainder of the discussion focuses on the 360 processors simulations. The boundaries between processors are message passing interfaces so that when a molecule crosses from processor A to B, all of its properties are passed from A to B. The pole-ward boundaries are essentially singularities. Each processor simulates 21,600 cells and approximately 10 molecules per cell are needed to give adequate statistics implying a minimum of $\sim 2 \times 10^5$ molecules per processor. In fact, to yield adequate statistics at high altitudes, many more than $\sim 2 \times 10^5$ molecules per processor are needed because the molecules are distributed non-uniformly with altitude (and the grid spacing is uniform above ~30 km) with the majority of molecules in the cells near the surface. In the simulations presented, about 10 million molecules are used per processor. The data are also time-averaged over the last 250 s of the simulation to decrease noise. Time-averaging is justified because the solution varies slowly in time and the time-average duration is much less than Io's rotational period of 42 h. For each of the final data sets, $\sim 10^{12}$ molecules are sampled throughout the entire domain.

3.3. Inhomogeneous surface model

Douté et al. (2001) determined the SO_2 surface frost distribution based on the IR emission from Io's surface. Their fraction of frost covering the surface is given with 1° resolution in both latitude and longitude. There were no data available between longitudes of 0°W and approximately 60°W because these longitudes were not observed. Results at polar latitudes have a low degree of reliability because of the highly oblique viewing angle. We obtained an electronic version of the data on the frost fraction from Sylvain Douté and, where no data were available, we computed the frost fraction using a linear interpolation scheme between 0°W and 60°W and pixel by pixel for polar latitudes. The resulting surface frost fraction utilized in the present work is shown in Fig. 2. Notice that the frost fraction is quite low in the linearly interpolated region because the frost fractions on the edges of the observed domain at 0°W and 60°W are low. There are two large regions of high frost concentration on the anti-jovian side at 50°N and 260°W and also at 60°S and 240°W. Both are regions where no large "persistent" volcanoes exist; however, these regions show a longitudinal correlation with the distribution of plumes at lower latitudes (Douté et al., 2001; Geissler et al., 2004; Marchis et al., 2005). A region at 310°W and 10°N with a very low frost concentration corresponds to the location of Loki.

The rock and frost covered areas within each surface pixel are assumed to be separate and discrete (with a length scale on the order of kilometers). Lateral heat conduction between rock and frost covered areas is thus assumed to be negligible as the vertical heat fluxes into the top layer of the surface (with a length scale on the order of centimeters, Kerton et al., 1996) will dominate any lateral heat fluxes. Each area element has its own independent temperature based on the emissivity, ε (assumed to be unity for both the frost and rock, similar to the value of 0.9 used by Veeder et al. (1994) and Kerton et al. (1996)), and thermal parameter, Mc, of that surface type. Mc (Saur and Strobel, 2004) is a thermal parameter derived by fitting to 20 and 30 μm radiance observations (Sinton and Kaminski, 1988). The latent heats of sublimation and

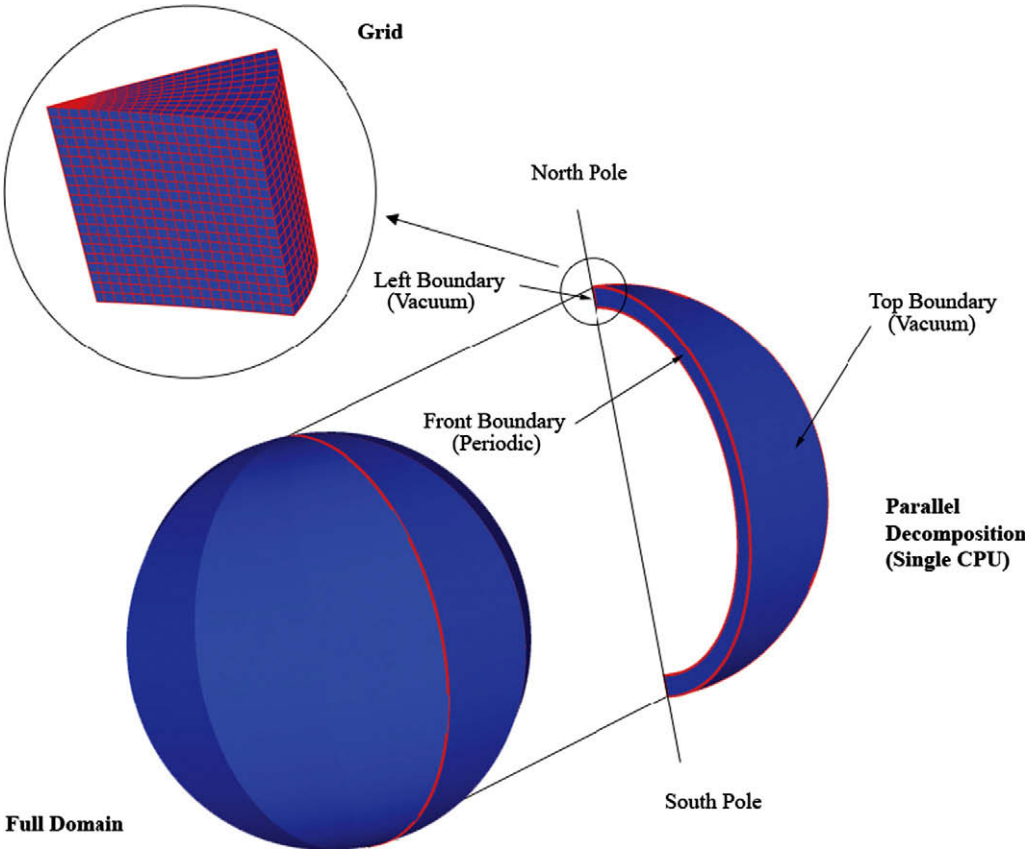

Fig. 1. Decomposed spherical domain with relevant boundaries labeled. The full domain is in the lower left corner and single processor's domain is extracted (right) to show the geometry of the domain decomposition. To the upper left is an enlarged view of the north pole of a single processor showing the cell structure. The azimuthal domain shown for a single processor is exaggerated for clarity.

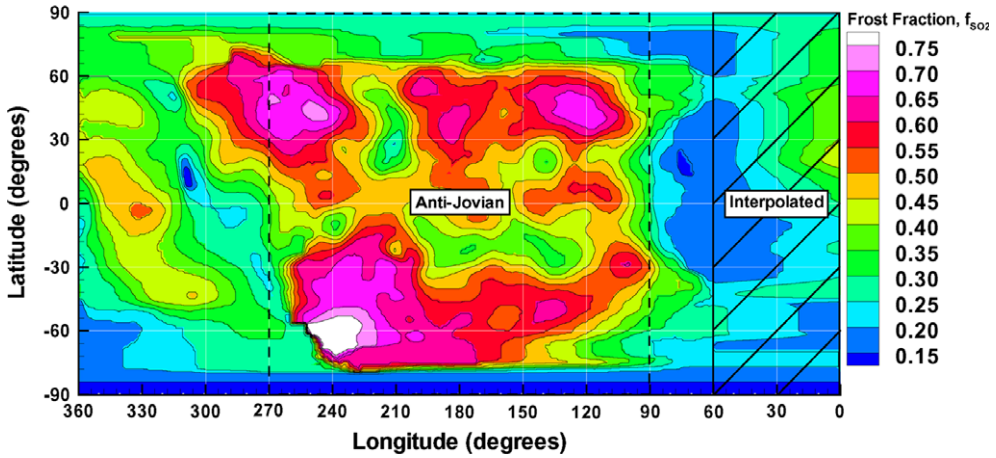

Fig. 2. Contours of the fractional coverage of surface frost, f_{SO_2}, as obtained from Douté et al. (2001). The cross-hatched area indicates longitudes that are linearly interpolated. The dashed rectangle from 90° to 270° encloses the anti-jovian hemisphere.

condensation are currently neglected as minor effects compared to the thermal inertia (Ingersoll et al., 1985; Kerton et al., 1996). The frost coverage fraction, f_{SO_2}, was used to modify the number of SO_2 gas molecules sublimated from surface frost. The sublimation rate of SO_2 molecules, N_{sub} [$(m^2\ s)^{-1}$], is given by.

$$N_{sub} = \frac{P_{vap}}{\sqrt{2\pi k_B T_s M_{SO_2}}} \tag{1}$$

where M_{SO_2} (kg) is the molecular mass of SO_2, k_B is the Boltzmann constant, the equilibrium vapor pressure, P_{vap} (Pa), is (Wagman, 1979)

$$P_{vap} = 1.516 \times 10^{13} e^{\frac{-4510}{T_s}} \tag{2}$$

and the surface temperature, T_s (K), is determined by solving the radiative balance equation

$$\frac{dT_s}{dt} = \begin{cases} \frac{\varepsilon\sigma}{Mc}\left(T_{s,eq}^4 - T_s^4\right) & \rightarrow \ dayside \\ \frac{\varepsilon\sigma}{Mc}\left(T_{\min}^4 - T_s^4\right) & \rightarrow \ nightside \end{cases} \quad (3)$$

Here σ is the Stefan–Boltzmann constant, $T_{\min}$ is the minimum (frost and rock) temperature, and $T_{s,eq}$ is an idealized radiative equilibrium solution for the surface temperature distribution (and the initial condition for Eq. (3)) defined by

$$T_{s,eq} = (T_{ss} - T_{\min}) \times \cos^{1/4}(\psi) + T_{\min} \quad (4)$$

where ψ is the solar zenith angle. The minimum temperature $T_{\min}$ is assumed to be 90 K based on the observations by the Galileo PPR (Spencer et al., 2000; Rathbun et al., 2004). The surface temperature distribution tends toward the equilibrium solution $T_{s,eq}$ but differs from it because of the thermal inertia of the surface.

The value of $T_{s,eq}$ at the subsolar point is defined to be T_{ss} (the subsolar temperature) and is the maximum possible temperature, but this is not the value of the frost surface temperature at the subsolar point due to the thermal inertia of the SO_2 frost. T_{ss} is parameterized to be either 120 K or 115 K. The actual peak T_{frost} is calculated to be 114.3 K when T_{ss} = 115 K and 119.1 K when T_{ss} = 120 K. As will be seen later, a subsolar temperature of 115 K yields column densities that agree with the lower bound of Lyman-α observations (Feaga et al., 2009). A 120 K subsolar temperature yielded column densities that are approximately five times larger and are above the upper range of observations (Jessup et al., 2004; Spencer et al., 2005). The 120 K case serves as an upper limit on possible circumplanetary flow strengths. The thermal parameter, *Mc*, is chosen independently for the frost and rock surfaces, with *Mc* chosen to be 3500 J K^{-1} m^{-2} for frost and 388 J K^{-1} m^{-2} for rock. The values of *Mc* for frost and rock are chosen to approximately match the nightside cooling rate of the brightness temperature seen in Galileo PPR observations (Rathbun et al., 2004). Currently, our model cannot simultaneously match both the observed nightside cooling rate and the longitudinal lag between the subsolar point and the location of the peak frost temperature (Rathbun et al., 2004). A more comprehensive surface temperature model that can match both of these parameters is in development.

Due to its higher thermal inertia, the frost surface warms and cools more slowly than the rock surface. The frost does not reach its peak temperature until ~32° of rotation (or 3.5 h) after the subsolar point as seen in Fig. 3b and c. Because of this lag, the frost surface has only cooled to approximately 110 K at the dusk terminator. The exponential decrease of the frost surface temperature continues throughout the nightside and it is only just before dawn that T_{frost} cools to within 1 K of the surface rock that is at 90 K. The rock temperature has a much lower thermal inertia and therefore follows radiative equilibrium closely (Fig. 3a). The lower thermal inertia causes the rock temperature to reach its peak temperature only 4° of rotation (or 30 min) after the subsolar point, and it cools correspondingly quickly after dusk.

In addition to scaling the number of computational molecules sublimated from the surface, the frost fraction is used to determine the probability of a molecule landing on rock or frost if it hits the surface. If a molecule lands on a frost covered surface, it is deleted from the computation, while a molecule landing on a rock surface will remain stuck to the surface for a period of time (a residence time) dependent on the surface temperature. Molecules landing on the frost covered areas are deleted because the sticking coefficient is defined to be unity for the vapor pressure model we use (Wagman, 1979) and the sublimated flux should model any (indistinguishable) molecules that would be re-emitted from the frost surface. Due to memory limit issues, the exact location of molecules stuck to the rocky surface is not retained. Instead, resident molecules are re-emitted randomly throughout the 1° × 1° cell in which they hit the surface. The residence time on the rock surface (in s) is

$$t_{res} = \frac{e^{\Delta H_s/k_B T_s}}{\nu_0} \quad (5)$$

where $\nu_0 = 2.4 \times 10^{12}$ s^{-1} is the lattice vibrational frequency of SO_2 within its surface matrix site and ΔH_s ($\Delta H_s/k_B$ = 3460 ± 40 K) is the surface binding energy of SO_2 on a surface of its own frost (Sandford and Allamandola, 1993). The two constants ΔH_s and ν_0 assume a monolayer or more of SO_2 covering the rock surface. A longer residence time is also modeled that is a thousand times longer than the short residence time given by Eq. (5) for SO_2 on SO_2 frost. The higher value represents residence times that could possibly occur with a highly porous surface (Matson and Nash, 1983) where molecules undergo multiple reflections before being emitted into the atmosphere.

The residence time of an SO_2 molecule on rock (based on Eq. (5)) on the cold nightside (90 K) is ~2×10^4 s which is over a quarter of Io's night (~7.5×10^4 s) and therefore most molecules that fall on the nightside rock will desorb at least once before dawn. The molecules stuck to the rock surface will be partially replenished by the thin nightside atmosphere. For the long residence time model, the residence time at 90 K is ~2×10^7 s and therefore nearly all the sublimated gas which falls on the nightside rock will remain stuck until dawn. At dawn the rock surface warms quickly and the residence time shortens dramatically to a few seconds (for the short residence time of SO_2 on the rock surface) and to approximately one and a half hours (for the long residence time). As a result, the atmospheric density is *enhanced* near the dawn terminator by molecules desorbed from the warming rock surface. For the short residence time model the rapid rate of warming causes the enhancement to occur in a small band (~10° in longitude) stretching from pole to pole. This enhancement occurs over a much larger area (nearly the entire morning side) for the long residence time model. We refer to this outflux as the dawn atmospheric enhancement. Compared to the long residence time model, the total density enhancement on the dayside will be smaller in the short residence time model. This is because the amount of SO_2 stuck to the rock is depleted at dawn because residence time is short compared to the duration of night whereas nearly everything remains stuck in the long residence time model; however, these desorptions during the night also tend to increase the nightside atmosphere (in the short residence time model).

3.4. Initial conditions

Io's atmosphere varies slowly in time when the effects of planetary rotation and non-uniform frost coverage are included. However, different physical time scales are relevant as the simulation approaches the final quasi-steady result. The time scales relate to (i) the thermal distribution of Io's surface, (ii) the distribution of SO_2 temporarily stuck to the rocky surface areas, and (iii) the gas dynamics of the full collisional molecular atmosphere. The quasi-steady state atmosphere for all cases is thus computed via a three step process. In step (i), the surface temperature distributions are determined with no atmosphere present. The temperature distributions of the surface frost and rock are obtained from Eq. (3) with appropriate values of *Mc* for rock and frost respectively, and allowed to relax to a steady state over three rotations of Io.

The quasi-steady state rock surface temperature distribution (shown in Fig. 3c) computed in step (i) allows for the computation of the appropriate SO_2 surface frost density (cm^{-2}) on the rock surface based on the frost coverage and time of day. In step (ii), the number of molecules stuck on the rock is determined by

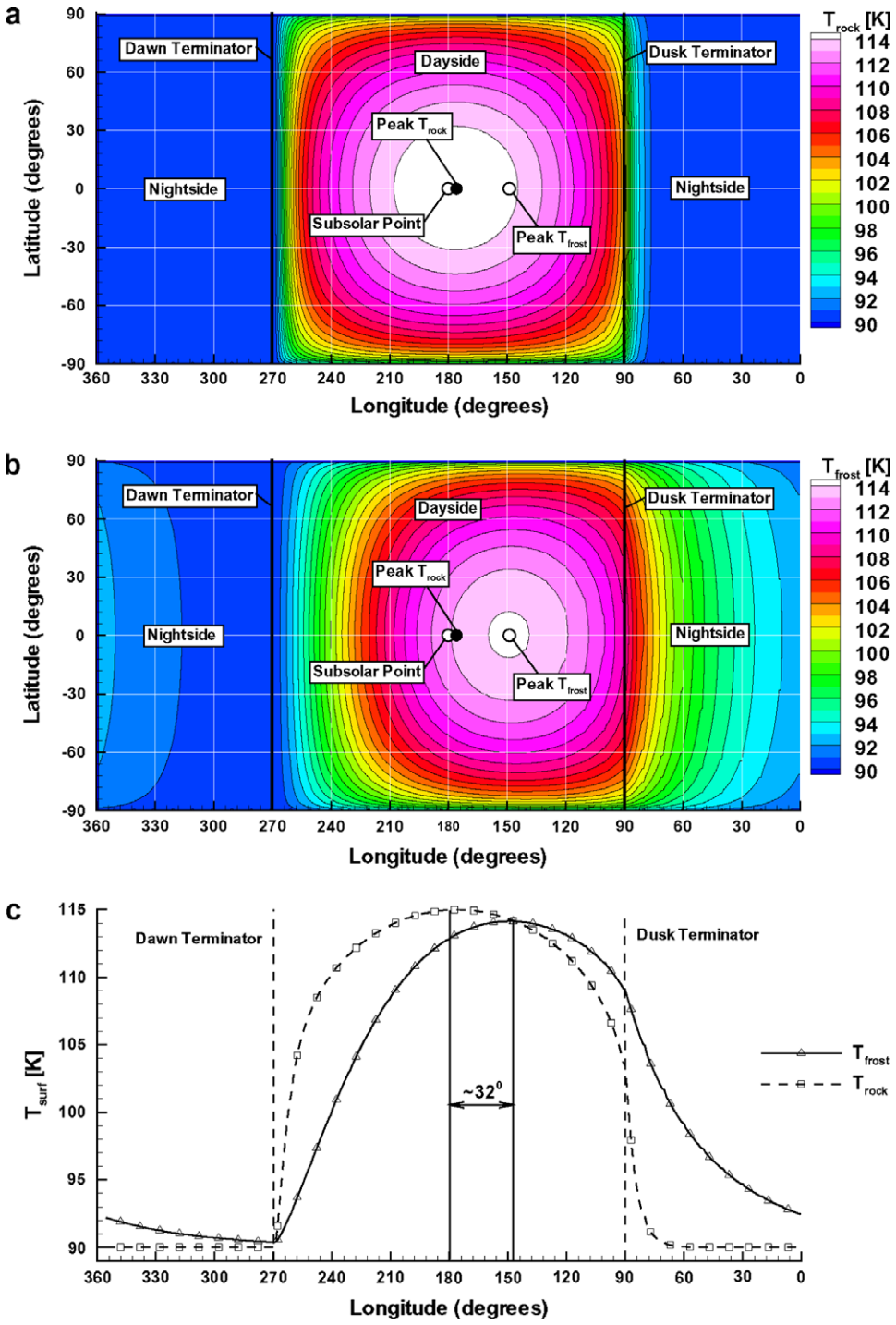

Fig. 3. Color contours of (a) surface rock temperature (T_{rock}) and (b) surface frost temperature (T_{frost}) as a function of latitude and longitude. (c) T_{frost} and T_{rock} at the equator as a function of longitude. The subsolar longitude is 180° for all cases. (For interpretation of the references to color in this figure legend, the reader is referred to the web version of this article.)

simulating a very low number of molecules (~100,000 per processor) without collisions. A quasi-steady state is achieved rapidly by using this relatively small number of molecules. Time-averaging of this solution yields adequate statistics for the SO_2 surface frost density on the rock surface. The rock surface boundary condition (i.e. the SO_2 number density stuck to the rock surface) is allowed to relax to steady state over one Io rotation.

With the surface boundary conditions now fully determined, the final quasi-steady atmosphere can be obtained by "cloning up" the molecules used to obtain the surface rock boundary condition. The ~100,000 molecules are "cloned up" to $\sim 10^6$ molecules by altering the weighting function (the number of real molecules each simulated molecule represents). Collisions are turned on in step (iii) and relaxation is allowed to occur for about 30 min of rotation which is long enough for cloned molecules to travel through several ballistic trajectories and thereby allow the cloned molecules' spatial positions and velocities to diverge through randomization at the surface. The simulation then progresses for ~ 4 h

until the atmosphere is near a final quasi-steady state. In the last step, the $\sim 10^6$ molecules are "cloned up" to $\sim 10^7$ molecules to decrease the statistical noise and allowed to further randomize over $\sim$30 min of rotation. This three step process reaches quasi-steady state at least an order of magnitude faster than beginning the calculation with a full complement of colliding molecules and computing a full Io rotation. The atmosphere is in a final quasi-steady state when the gas properties such as temperature and density have only small time variations attributable to the slowly changing surface temperature as Io rotates.

3.5. Load balancing

Io's atmosphere has large column density variations which in DSMC could result in large variations in the number of molecules per cell. Because of the large scale nature of the calculation, the maximum number of molecules per cell is limited to $\sim$100. Since the density varies over five orders of magnitude in the domain, 100 representative molecules in the highest density cell would mean that many cells would on average have zero molecules present. This statistical issue necessitates the use of a spatially variable particle weighting function. The weighting function adjusts the ratio of computational particles to real particles in every column of cells based upon the surface area and surface temperature of the cell at the base of the column. When a particle passes from one cell to a neighboring cell with a different weight, it is cloned or destroyed depending on the ratio of the two cell weights. For more details on weighting functions, see Bird (1994). We have been careful when using weighting functions because they do not conserve mass, momentum, and energy exactly; however, in the limit of large molecule numbers, they are conservative on-average. The weighting function is implemented such that each column of cells will have the same number of computational molecules at each time step. This is necessary because of the geometry of the spherical coordinate system as well as the large variations in density.

3.6. Calculation of vibrational temperatures

The calculation of the gas vibrational temperature in the ν_2 vibrational mode of SO_2 is computationally difficult because the atmosphere in certain areas (especially areas where the plasma does not reach) is quite cold (<90 K). The vibrational temperature is calculated from (Bird, 1994):

$$T_{vib} = \frac{T_{ch}}{\ln(n_0/n_1)} \tag{6}$$

where T_{vib} is the vibrational temperature, T_{ch} is the characteristic temperature of the vibrational mode, n_0 is the number of molecules in the ground state, and n_1 is the number of molecules in the first excited state. Although vibrational levels above the first excited state are modeled in our code, such states are exceedingly rare in our simulations and we will assume that they can be neglected for purposes of computing the minimum resolvable gas temperature. The total number of molecules in a cell is then equal to the sum of molecules in the ground state and the first excited state based on this assumption. Then the vibrational temperature can be re-written as:

$$T_{vib} = \frac{T_{ch}}{\ln((N-n_1)/n_1)} \tag{7}$$

The minimum vibrational temperature which can be resolved for a total number of molecules per cell, N, can be calculated if we suppose $n_1 = 1$ (i.e. the lowest possible non-zero vibrational temperature which our simulation can compute occurs when only one molecule out of N is excited and the rest are in the ground state). Substituting for $n_1 = 1$ into Eq. (7):

$$T_{vib} = \frac{T_{ch}}{\ln(N-1)} \tag{8}$$

A reasonable estimate for the maximum feasible number of molecules per cell that can be sampled (assuming a time-average over 500 time steps and $\sim$500 instantaneous molecules per cell) is $N \approx 2.5 \times 10^5$. Since we use a time step ($\Delta t = 0.5$ s) larger than the mean collision time (and time to cross a cell) in the lower atmosphere, the molecule properties are sufficiently randomized each time step such that each sample is likely unique. The characteristic temperature of the ν_2 vibrational band of SO_2 is $T_{ch} = 745$ K. For these values, the minimum vibrational temperature that can be resolved is $\sim$60 K. As the vibrational temperature we wish to resolve decreases, the number of molecules needed to resolve that vibrational temperature increases exponentially. Luckily, the coldest temperatures in the dense atmosphere do not drop much (<5 K) below 60 K (confirmed by temporally and spatially resolved one-dimensional DSMC simulations) and therefore we can compute vibrational temperatures by time-averaging runs such that the total number of particles per cell is sufficient. We are not presently able to resolve cold vibrational temperatures above 100 km in altitude because the number of particles per cell drops below the required threshold and the samples become non-unique.

3.7. Superposition of volcanic plumes on the sublimation atmosphere

Since the relative contribution of volcanic plumes to Io's atmospheric column is non-negligible, especially locally, it is reasonable to assume that they should affect the observed disk-averaged ν_2 vibrational band of SO_2 at 19.3 μm. Therefore, pre-computed volcanic plumes were superimposed on the simulated sublimation atmosphere (see Fig. 4) and their effect on the disk-averaged band depth was investigated with a backwards Monte Carlo radiative transfer code in a companion paper (Gratiy et al., 2009). The model uses ten volcanoes, listed in Table 1. Unfortunately, there is no comprehensive list of plume activity during Spencer et al.'s (2005) observations and so we chose the plumes based on their activity during the Galileo mission. We exclude highly episodic plumes (such as Tvashtar) and superimpose onto the sublimation atmosphere only those plumes that were generally active throughout the Galileo observations. We use Geissler et al.'s (2004) timeline of plume activity based on observed surface changes to determine the plumes that were "consistently" active throughout Galileo (Table 1).

The volcanic plumes were computed separately using the same DSMC code in a smaller domain centered on the volcanic vent on a very finely resolved grid (Zhang et al., 2003). The volcanoes were then superimposed onto the simulated sublimation atmosphere by adding the volcanic plume number density to the sublimation atmosphere number density. The local velocity, translational, rotational, and vibrational temperatures are then all mass-averaged based on the respective contribution from the plume and sublimation atmosphere. Note that there is no self-consistent interaction between the global atmosphere and the superimposed plumes during the independent simulations of the plumes and the sublimation atmosphere.

The simulation uses two general volcanic types, each of which can be either dayside or nightside (when the sublimation atmosphere is minor). Dayside plumes (computed with a surface temperature of 112 K) are used when the sublimation atmospheric density near the surface is large enough that the gas falling to the surface from the canopy is turned via a re-entry shock above the sublimating atmosphere. When the sublimation atmosphere

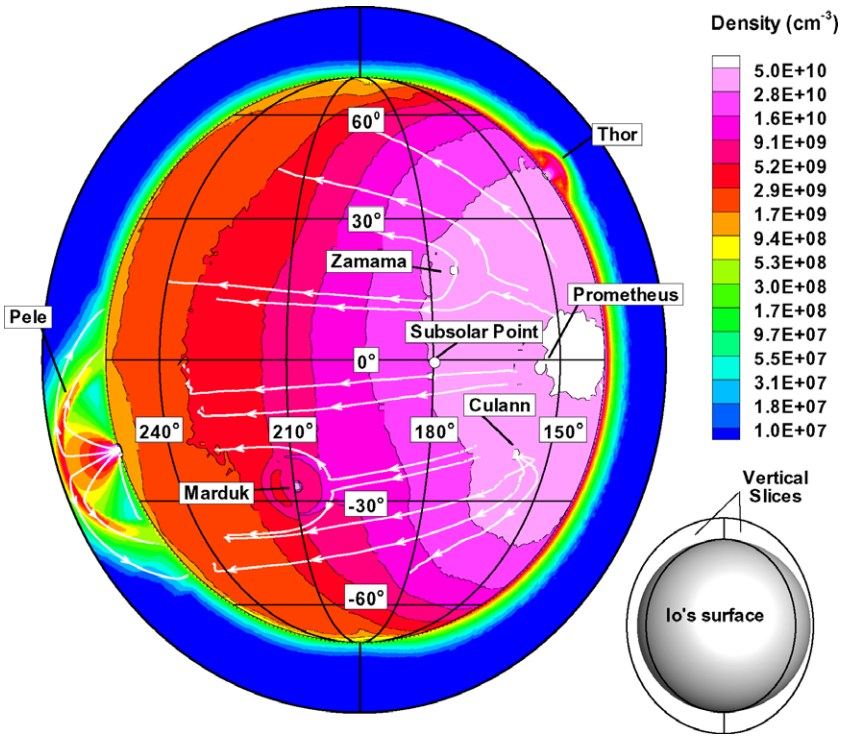

Fig. 4. The density of the superimposed baseline sublimation and volcanic atmospheres at ~100 m above the surface plus two near-limb slices showing the vertical density field. Note that the viewing angle has been altered so that Pele is visible (i.e. the subsolar point is not at the center of the disk) and that the slices showing the vertical density profile on either side of Io's disk were selected to cut through two plumes and are not on the limb, hence the surface seen is not the full disk (see inset). Streamlines (white) are shown to illustrate the gas flow in the plumes and the diversion of the circumplanetary winds around the plumes. The streamlines are seen to end near where net condensation begins as the gas flows into the surface.

Table 1
Active plume list (Geissler et al., 2004).

Plume	Longitude, latitude	Type
Kanehikili	40°W, 18°S	Prometheus
Masubi	55°W, 44°S	Prometheus
Amirani	115°W, 26°N	Prometheus
Thor	135°W, 40°N	Prometheus
Prometheus	155°W, 2°S	Prometheus
Culann	159°W, 20°S	Prometheus
Zamama	174°W, 18°N	Prometheus
Marduk	210°W, 27°S	Prometheus
Pele	258°W, 19°S	Pele
Loki[a]	309°W, 13°N	Prometheus

[a] Active, Rathbun et al. (2002).

is negligible (i.e. nightside at a T_{frost} of 90 K), the gas falls unimpeded from the canopy to the surface (Zhang et al., 2004). Each of the plumes is appropriately superimposed as a dayside or nightside plume depending on the plume's location and the local near-surface sublimation atmospheric density. We classify large volcanoes with a ring radius exceeding ~400 km and shock heights of several hundred kilometers as Pele-type plumes. The Pele-type plumes have a virtual vent temperature of 650 K, a velocity of 900 m/s, and a mass flow rate of 1.1×10^4 kg/s (Zhang et al., 2003). Smaller volcanoes are simulated as Prometheus-type plumes with a ring radius of ~180 km and a shock height of 120 km. Our Prometheus-type plumes have a virtual vent temperature of 300 K, a velocity of 500 m/s, and a mass flow rate of 5.9×10^3 kg/s.

3.8. Plasma heating

The plasma energy, originating in the jovian magnetospheric torus (Frank et al., 1996), is assumed to enter radially from the top of the domain uniformly over the entire satellite. Excitations of translational and rotational modes by the plasma are accounted for by depositing an equal amount of energy into each degree of freedom while vibrational excitation by the plasma is neglected for lack of a suitable model. The plasma energy flowing down through a column is depleted, dependent on the gas density, as it is absorbed by the gas in a given cell. The remaining energy travels down the column of cells until it is completely depleted or reaches the surface. For a detailed account of the plasma heating model, see Austin and Goldstein (2000).

The plasma energy flux is taken to be 5.0 erg s^{-1} cm^{-2} for all cases. Previous models have used a plasma energy flux of 1.3 erg s^{-1} cm^{-2} (Linker et al., 1988; Pospieszalska and Johnson, 1996; Austin and Goldstein, 2000) based on the fraction of plasma energy that reaches the exobase as opposed to that which is deflected around Io. We use a higher value as an upper limit on the plasma flux. A lower value of 1.0 erg s^{-1} cm^{-2} was found to negligibly alter the vertical density structure of the atmosphere (compared to 5.0 erg s^{-1} cm^{-2}) but did alter the vertical thermal structure (Moore et al., 2009); however, using a lower value of 1.0 erg s^{-1} cm^{-2} leads to problematic noise in the calculation of the 3D vibrational temperatures which is prohibitively expensive to circumvent computationally (see Section 3.6).

The plasma model used here is crude but is only a first step. A more advanced model is currently being developed which tracks individual ions and electrons as they move along magnetic field lines. It includes the momentum transfer from the plasma to the atmosphere, direct vibrational excitation of SO_2 molecules via collisions with ions and electrons, and a more accurate plasma energy distribution over Io's leading and trailing hemispheres. The discussion in Section 4.2 should be read with the understanding that the actual plasma impingement on Io's atmosphere is non-uniform and can lead to nearly an order of magnitude difference in the amount

of plasma energy which interacts with the atmosphere. This could significantly change the locations at which the plasma energy reaches the surface as well as the vertical thermal structure of the atmosphere.

4. Results

The effects on Io's atmosphere of planetary rotation, heating due to plasma bombardment, inhomogeneous surface frost, SO_2 residence time on rock, subsolar temperature, and volcanic plumes are examined for several subsolar longitudes. The atmosphere is simulated at six subsolar longitudes corresponding to 0°, 60°, 120°, 180°, 240°, and 300°W longitude. For each subsolar longitude, the column densities of the sublimation atmosphere with and without volcanic plumes are compared in the companion paper (Gratiy et al., 2009). The T_{ss} examined is either 120 K or 115 K. The value of 120 K yields column densities five times larger than the 115 K values and above the upper range of recently observed columns (Jessup et al., 2004; Spencer et al., 2005), while the lower temperature of 115 K was found to approximately agree with the lower range of observed columns (Feaga et al., 2009; McGrath et al., 2000). Each subsolar longitude is also simulated with a longer residence time of SO_2 on rock. The varied parameters for the three different atmospheric simulation cases are shown in Table 2.

The baseline simulation is chosen to be an atmosphere with T_{ss} = 115 K, 180° subsolar longitude, with the longer residence time, and no volcanic plumes included. An atmosphere with T_{ss} = 115 K and short residence time will hereafter be referred to as Case 2, and an atmosphere with T_{ss} = 120 K and a long residence time will be referred to as Case 3. Both Cases 2 and 3 are also at a subsolar longitude of 180°W and have no volcanic plumes included. Locations on Io will be given both in Iocentric longitude as well as local time of day for clarity. The reference points for the local time are: 6:00 am – dawn terminator, 12:00 pm – subsolar point, 2:08 pm – Peak T_{frost}, and 6:00 pm – dusk terminator.

4.1. Overall flow features

Circumplanetary flow develops as the high vapor pressure region near the peak T_{frost} pushes gas toward the low vapor pressure region on and near the nightside. Because the vapor pressure is exponentially dependent upon the surface temperature, the vapor pressure drops rapidly near the terminator. For the baseline atmosphere, the net sublimation region, where the vapor pressure is greater than the atmospheric pressure, is largely confined to a circular region around the peak T_{frost} (148°W or ~2:10 pm) but with an additional region on the morning side between 260–200°W (6:40–10:40 am) and 40°N–30°S due to the dawn atmospheric enhancement (see Fig. 5). For the baseline case, the sublimation region extends ~45° east of the peak T_{frost}, ~105° to the west, and ~60° to the north and south. For a case with an anti-solar temperature of 50 K and a subsolar temperature of 130 K Ingersoll et al. (1985) found that the net sublimation region extended ~37° away from the subsolar point. There is no direct comparison that can be made between our work and Ingersoll et al. (1985), but our sublimation region possibly extends further to the north, south, and west than Ingersoll et al. (1985) because their simulations had relatively cold temperatures near the terminator which would sublimate very little gas based on vapor pressure equilibrium likely creating regions of net condensation. The greater eastward extent of the sublimation region is due to the dawn atmospheric enhancement.

For the baseline atmosphere, condensation occurs nearly everywhere else on the dayside but primarily in a ring (~15–30° thick) near the terminator. The condensation is weaker near the dawn terminator because of the additional desorption of SO_2 molecules from the rocky surface, whereas these molecules have nearly all desorbed near the dusk terminator. Condensation occurs nearly everywhere on the nightside due to the circumplanetary flow which originates on the dayside and condenses on the nightside. There are small patches of mean sublimation on the nightside near the anti-solar point where the mean vertical velocity is slightly positive due to noise. When T_{ss} is increased from 115 K to 120 K (Case 3), the circumplanetary flow is enhanced considerably as expected. The higher T_{ss} leads to a much larger day-to-night pressure gradient than exists for the 115 K atmospheres. Also, the eastward extent of the sublimation region does not change significantly while the westward extent increases to higher latitudes on the morning side between 260°W and 240°W (6:40–8:00 am).

For the baseline atmosphere, the circumplanetary flow does not originate at the point of maximum vapor pressure, but instead at a point ~10° east (~2:40 pm) (Figs. 6 and 7a). The westward momentum of the column of gas above the region of peak pressure must be slowed by the momentum flux from the surface in order for the flow to re-equilibrate with the gas pressure and originate from the region of peak pressure. Because the timescale associated with reducing the momentum of the flow to zero is on the order of 1 h, there is a ~10° lag in the origin of the flow as Io rotates. The region of origin of the winds also varies between different subsolar longitudes because as Io rotates dayside frost fraction changes (and therefore the pressure field varies).

As flow diverges from the point of origin, it is accelerated toward the nightside by the high day-to-night pressure gradient and also pushed to higher altitudes by the upward momentum of the sublimation atmosphere (see Fig. 6). The winds are not directly away from the region of origin because the inhomogeneous surface frost alters the pressure field leading to a slight curvature of the streamtraces (see Fig. 7a). Irregular flows up to 50 m/s do develop where strong frost gradients occur. These irregular flows are more visible on the nightside where the surface temperature is nearly constant. Of course there the flow is nearly free molecular. The flow below 2 km altitude is subsonic near the dusk terminator (see Fig. 6). However, due to rarefied slip, the flow within 15 m of the surface at the equator near the dawn terminator remains supersonic. The difference in the low altitude Mach numbers between the dusk and dawn terminators is due to the higher pressure gradient that exists near the dawn terminator.

The pressure gradient between the warmest point on Io and the terminator is strong enough to drive the flow supersonic. For the baseline atmosphere at 30 km altitude, the flow is supersonic at all latitudes and longitudes around the terminator (Fig. 7a). As the gas flow passes onto the nightside, the density (and collision rate) drop to the point where the flow essentially becomes free molecular. The gas flow that has been accelerated to supersonic speeds then continues on ballistic trajectories through the thin nightside atmosphere until it condenses on the cold nightside surface. For Case 2, the flow goes supersonic at all latitudes and longitudes except near the dawn terminator (Fig. 7b). The difference between the two cases is explained by the dawn atmospheric enhancement. As discussed in Section 3.3, the magnitude of atmospheric column enhancement for the baseline atmosphere is extended over a much larger area than in Case 2, where the dawn

Table 2
Parameters for the three atmospheric cases.

Case	Residence time model	Peak T_{frost} (K)
1	Long	115
2	Short	115
3	Long	120

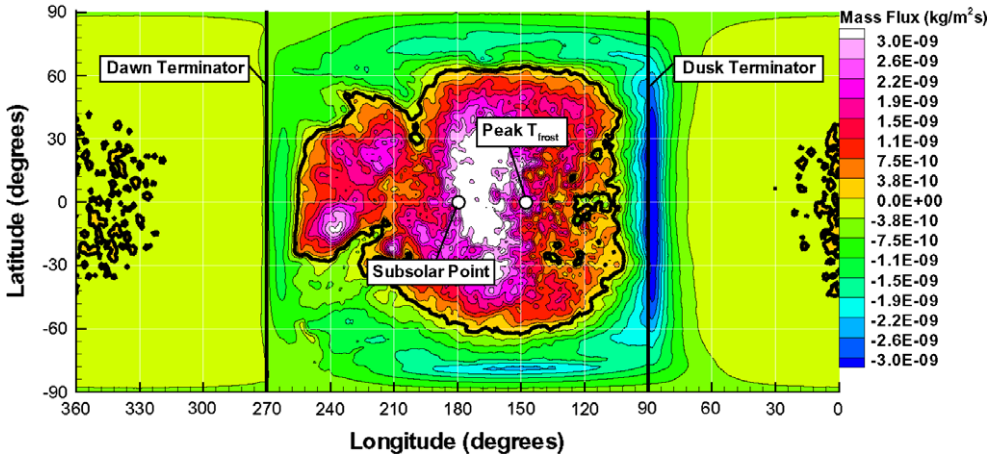

Fig. 5. The net mass flux of SO_2 gas from surface for the baseline atmosphere. The heavy black line contour denotes zero net mass flux. Areas of positive mass flux are regions of mean sublimation while areas of negative mass flux are regions of mean condensation. The mean mass flux within 60° longitude of the peak T_{frost} are higher in the west than in the east because of the underlying frost fraction.

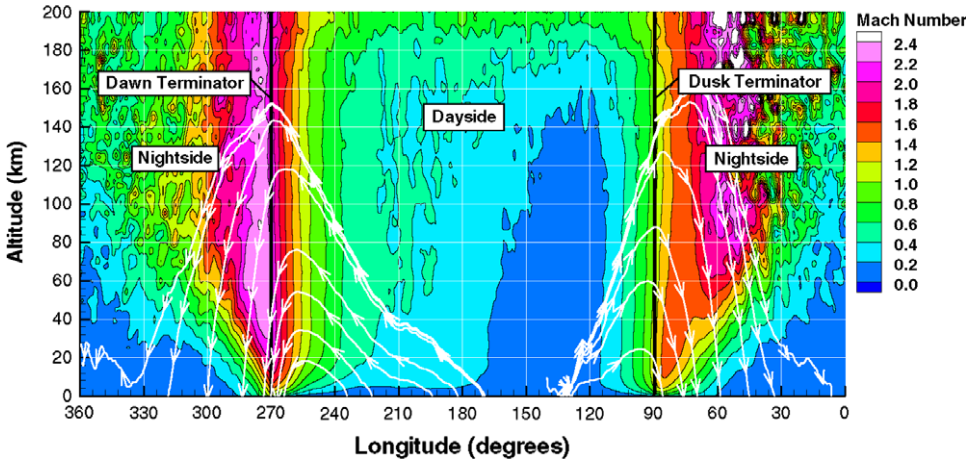

Fig. 6. Color contours of the Mach number for a cross-sectional slice through the atmosphere at the equator for the baseline atmosphere. Streamtraces showing the dayside to nightside flow are displayed in white. (For interpretation of the references to color in this figure legend, the reader is referred to the web version of this article.)

atmospheric enhancement occurs in a very small longitudinal band starting at the dawn terminator. The smaller but more pronounced enhancement of Case 2 is more efficient in blocking the westward flow (see streamtraces in Fig. 7b). For Case 3, the flow is similar to the baseline atmosphere but the strength of the flow increases due to the higher pressure gradient (see Fig. 7c).

For the baseline atmosphere at 30 km near the equator, the westward flow goes supersonic at 250°W (7:20 am) and remains supersonic until 285°W (5:00 am). The eastward flow goes supersonic at 90°W (6:00 pm) until 60°W (8:00 pm). There are slight differences in these distances at low latitudes attributed to variations in the frost fraction (Fig. 7a). Near the poles, the north/south flow goes supersonic on the dayside at 70°N/S, respectively, and remains so until the same latitudes on the nightside. For Case 2 at 30 km near the equator, the westward flow first goes supersonic at 205°W (10:40 am) and remains supersonic until 250°W (7:20 am). At 250°W, the flow is blocked by the dawn atmospheric enhancement. The eastward flow goes supersonic at 90°W (6:00 pm) until 70°W (7:20 pm). The difference in the extent of the eastward supersonic flow between the baseline and Case 2 atmospheres is again explained by the different residence time models. As discussed in Section 3.3, molecules do not remain stuck for the entire night (in the short residence time model) and therefore the nightside atmosphere is thickened by these molecules desorbing from the surface. The thickened atmosphere *decreases* the day-to-night pressure gradient and reduces the Mach numbers in all directions. Near the poles, the north/south flow goes supersonic on the dayside at 75°N and 70°S, respectively, until ~75° on the nightside. The north/south flow has a slightly larger extent in the baseline atmosphere than Case 2. For Case 3, the supersonic regions near the equator at 30 km occur largely in the same regions as the baseline atmosphere. The flow travels approximately 4300 km to the dawn terminator and only about 1400 km to the dusk terminator from its point of origin (at ~140°W or 2:40 pm).

The Mach number increases with altitude up to the top of the domain. For the baseline atmosphere, at an altitude of 30, the peak Mach numbers have equatorial values of $M = 2.20 \pm 0.05$ near the dawn terminator and 1.50 ± 0.05 near the dusk terminator. The error estimates are based on noise fluctuations in adjacent cells. The Mach number varies around the supersonic region near the terminator due to the variations in pressure caused by variations in the surface frost coverage and also the dawn atmospheric enhancement. Regions of low frost coverage tend to enhance the local Mach number while regions of high frost tend to decrease the local Mach number. The north/south flow is stronger in magnitude than the east/west flow and also varies because of the inhomogeneous sur-

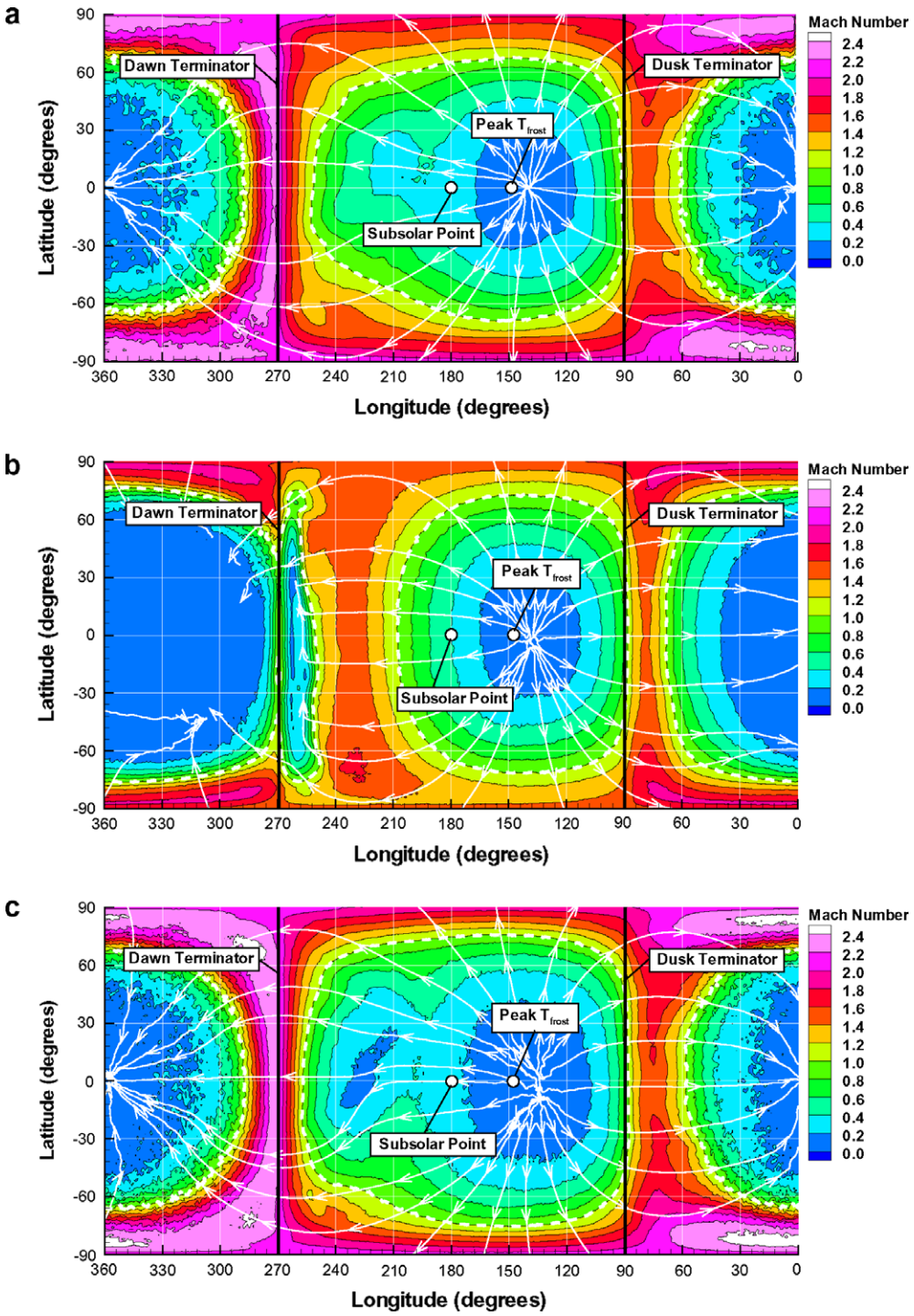

Fig. 7. Color contours of the Mach number at an altitude of 30 km as a function of latitude and longitude for (a) the baseline atmosphere, (b) Case 2, and (c) Case 3. The dawn and dusk terminators are denoted by the thick black vertical lines. Streamtraces (in white) track the flow away from ~135°W toward the nightside for the baseline atmosphere. Note that much of the curvature of the streamtraces is due to projection effects. The sonic line is shown by the dashed white line.

face frost. The north/south flow is stronger than the east/west flow because of the higher north/south pressure gradient. Flow to the east is accelerated by a smaller pressure gradient since the frost remains warm well after dusk (6:00 pm). Flow to the west is relatively stronger because the frost is cold (90 K) just before dawn (6:00 am) and therefore the pressure gradient is nearly equal to the north/south flow. The only difference between the north/south flow and the westward flow is the underlying frost fraction which is lower near the poles and leads to a slightly increased pressure gradient to the north and south. At the longitude of the peak T_{frost}, the maximum Mach number of the northern flow is ~2.30 while the southern flow at the same longitude has a maximum Mach number of ~2.42. The southern flow is faster than the northern flow because the (interpolated) frost fraction (and hence the pressure) is lower near the south pole than the north pole.

For Case 2, the flow Mach number near the dawn terminator is closer to that found near the dusk terminator for this case because the dawn atmospheric enhancement blocks the westward flow

(effectively keeping the flow from being accelerated to the high Mach numbers seen in the baseline case). The westward flow away from the dawn atmospheric enhancement is nearly supersonic (at 270°W; 6:00 am) and reaches a magnitude of $M = 0.95$ because the pressure is very high compared to the nearby nightside (and early morning dayside) vapor pressures. The shorter residence time smoothes the inhomogeneities caused by the surface frost coverage and also leads to slightly higher densities (on the evening side) as many molecules are desorbed quickly from the warm rock on the dayside. In Case 2, the morning side densities tend to be lower than the baseline case. This is because the dawn atmospheric enhancement covers most of the morning side (in the baseline case), whereas the dawn atmospheric enhancement is confined to a thin region near the dawn terminator (in Case 2). The higher densities on the evening side do not result in higher eastward Mach numbers compared to the baseline case, because of the thickened nightside atmosphere. The peak Mach number on the equator at 30 km altitude is 1.48 ± 0.05 near the dawn terminator and 1.41 ± 0.05 near the dusk terminator. The variation in the Mach number around the terminator is also decreased because the pressures are more uniform around the ring.

For Case 3, at the equator, the Mach number is ~2.34 near the dawn terminator and ~1.56 near the dusk terminator. The difference in Mach number between the two terminators is due to the thermal inertia of the frost which decreases the pressure gradient toward the dusk terminator. The north/south flow is similar in morphology to the baseline case but has slightly elevated values due to the increased pressure gradient at 120 K.

For the long residence time atmospheres, the Mach numbers change significantly as a function of subsolar longitude as Io rotates. The mean surface frost fraction on the dayside changes as the subsolar longitude varies (Fig. 8), resulting in stronger or weaker day-to-night pressure gradients. The Mach number tends to increase near either terminator when a region of low mean frost fraction is near that terminator (as this increases the pressure gradient which drives the flow), and to decrease near regions of high mean frost fraction. For the short residence time atmospheres, the Mach numbers tend to be larger at all subsolar longitudes compared to the corresponding long residence time atmosphere. The short residence time atmospheres also exhibit smaller variations in the Mach number as a function of subsolar longitude due to smaller variations in the pressure field compared to the long residence time atmospheres.

4.2. Translational, rotational, and vibrational temperatures

Fig. 9 shows color contours of translational temperature, T_{trans}, in a cross-sectional slice of the atmosphere through the equator for the baseline atmosphere. The increase in translational temperature near the dusk (90°W or 6:00 pm) and dawn (270°W or 6:00

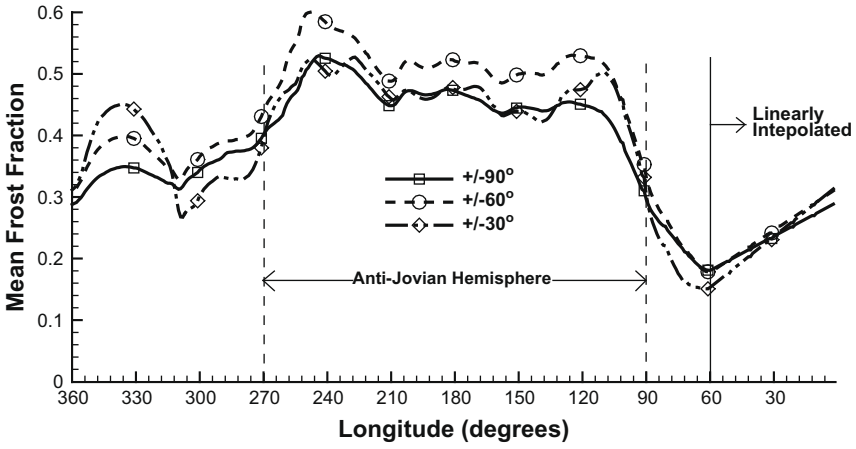

Fig. 8. The latitudinally averaged frost fraction as a function of longitude. Three different averages were considered: between ±30°, ±60°, and ±90° latitude (i.e. from pole to pole). The anti-jovian hemisphere has a higher mean frost fraction than the sub-jovian hemisphere for all cases.

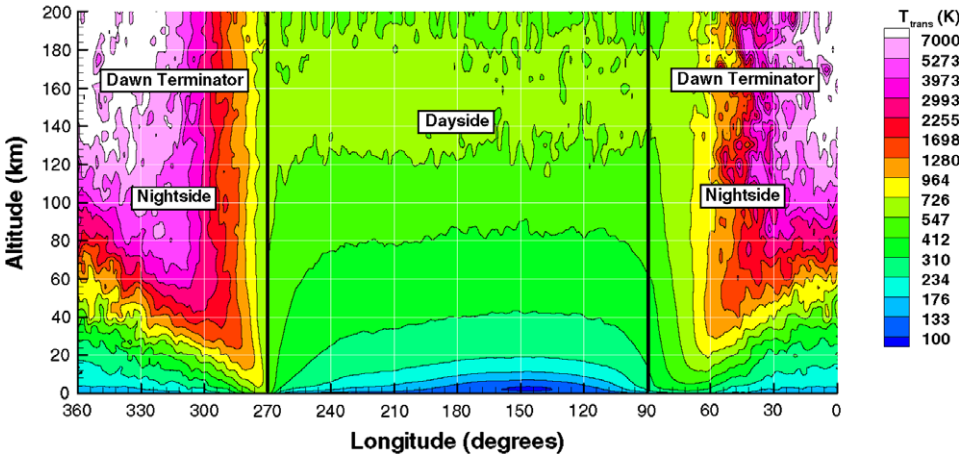

Fig. 9. Contours of T_{trans} for a cross-sectional slice through the atmosphere at the equator for the baseline atmosphere.

am) terminators corresponds to a non-equilibrium region. The temperature increase is due to the accelerated gas flows which originated on the dayside falling down through the thin upwelling nightside atmosphere (see streamtraces in Fig. 6). T_{trans} exhibits an interesting structure due to the plasma heating model for the baseline atmosphere. Near the surface, T_{trans} closely tracks T_{frost} because the SO_2 gas is nearly in thermodynamic equilibrium with the surface (Fig. 9). Below 2 km altitude at the location of the peak T_{frost} (148°W or ~2:10 pm) the sublimated SO_2 gas is radiating vibrationally and rotationally as it travels upward and spreads laterally (Moore et al., 2009). Above 2 km altitude, T_{trans} increases with altitude due to the plasma heating, despite the gas continuing to expand and radiate. For these two reasons, the lower atmosphere around 150°W has a volume of cold gas bracketed above and below by warmer gas (as seen in Fig. 10). Above 2 km, T_{trans} becomes dependent upon the plasma energy flux reaching that location. The column is much thicker above the peak T_{frost} region, so the plasma energy flux is absorbed by the upper atmosphere (above 2 km), leaving the lower atmosphere unaffected as seen in Fig. 9 and 11a. The altitude at which the plasma is completely absorbed by the atmospheric column decreases away from the region of peak T_{frost} (because the column decreases).

For Case 3, the thermal structure of the atmosphere is similar in morphology, but the altitude at which complete plasma depletion occurs is higher everywhere on the dayside because of the increase in column. The thicker column leads the plasma depletion altitude directly above the peak T_{frost} to increase from 2 km (for the baseline atmosphere) up to 5 km. The cool gas (bracketed between the surface-warmed gas and the plasma-warmed gas) above the peak T_{frost} for the T_{ss} = 120 K atmosphere cools to much lower temperatures (as low as 50 K) than for the T_{ss} = 115 K cases because of the strong gas dynamic expansion and emission of radiation.

Fig. 11a shows that T_{trans} at 4 km altitude is approximately 100 K near the region of peak T_{frost}; the SO_2 gas is sublimated in thermal equilibrium with the surface, cools while it radiates and expands laterally up to ~2 km, and is then plasma heated partially back to its original temperature in the remaining 2 km. At 4 km altitude, (over the region of peak T_{frost}) T_{trans} *increases* as T_{frost} (and therefore column) *decreases* because the plasma penetrates deeper into the atmosphere. At 4 km altitude near the equator, T_{trans} is ~300 K at 260°W (6:40 am) but rises to ~700 K at 275°W (5:40 am). The 233% T_{trans} increase between these two locations is due to a non-equilibrium region on the nightside from two gas flows passing through each other without collisions. T_{trans} near the dusk terminator is lower because the flow is weaker and therefore gas flow streaming down through the thin sublimation atmosphere creates a weaker non-equilibrium region. Additionally, T_{trans} is higher near the poles due to the stronger flows that exist there. Case 2 (Fig. 11b) is similar to the baseline case near the dusk terminator; however, the temperatures there are lower due to the weaker flows compared to the baseline case. There are significant differences between Case 2 and the baseline case near the dawn terminator. The dawn atmospheric enhancement creates a region of stagnant flow and therefore T_{trans} is dependent only on the plasma heating. T_{trans} in this region (265°W or 6:20 am) is ~210 K. In the region to the east of the dawn atmospheric enhancement near the equator (255°W or 7:00 am), where the westward flow is still supersonic, T_{trans} peaks at ~375 K. T_{trans} near the poles is also correspondingly cooler compared to the baseline atmosphere due to the weaker north/south flows that exist in Case 2.

For Case 3 (as seen in Fig. 11c), the morphology is similar to the baseline atmosphere. T_{trans} near the terminator tends to be higher (than the baseline atmosphere) because of the stronger flows and hence stronger non-equilibrium regions. Conversely, T_{trans} (at 4 km altitude) near the peak T_{frost} is quite low because of the increased altitude of plasma depletion.

The rotational temperature, T_{rot}, is maintained in equilibrium with T_{trans} by collisions; departures from thermal equilibrium occur because the collision rate drops as the density decreases with altitude. In the baseline atmosphere (T_{ss} = 115 K), T_{rot} is in equilibrium with T_{trans} at altitudes below 40 km on the dayside and nowhere on the nightside (Figs. 10, 12a, and b). As seen in Fig. 10,

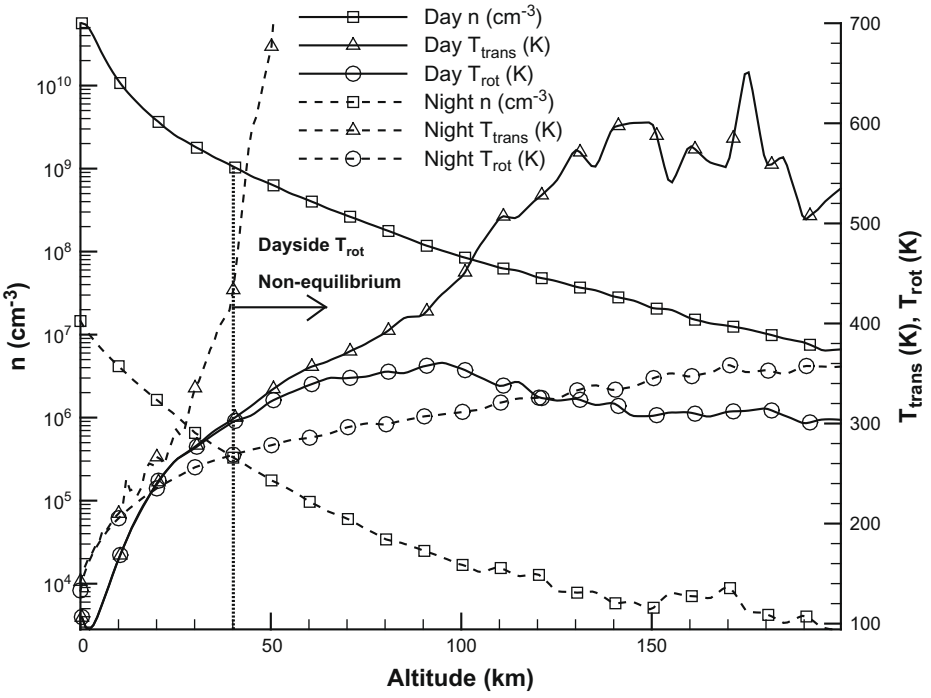

Fig. 10. T_{trans}, T_{rot}, and number density as a function of altitude at the equator for longitudes at the peak T_{frost} (dayside) and at 330°W (nightside) for the baseline atmosphere (subsolar longitude of 180°W).

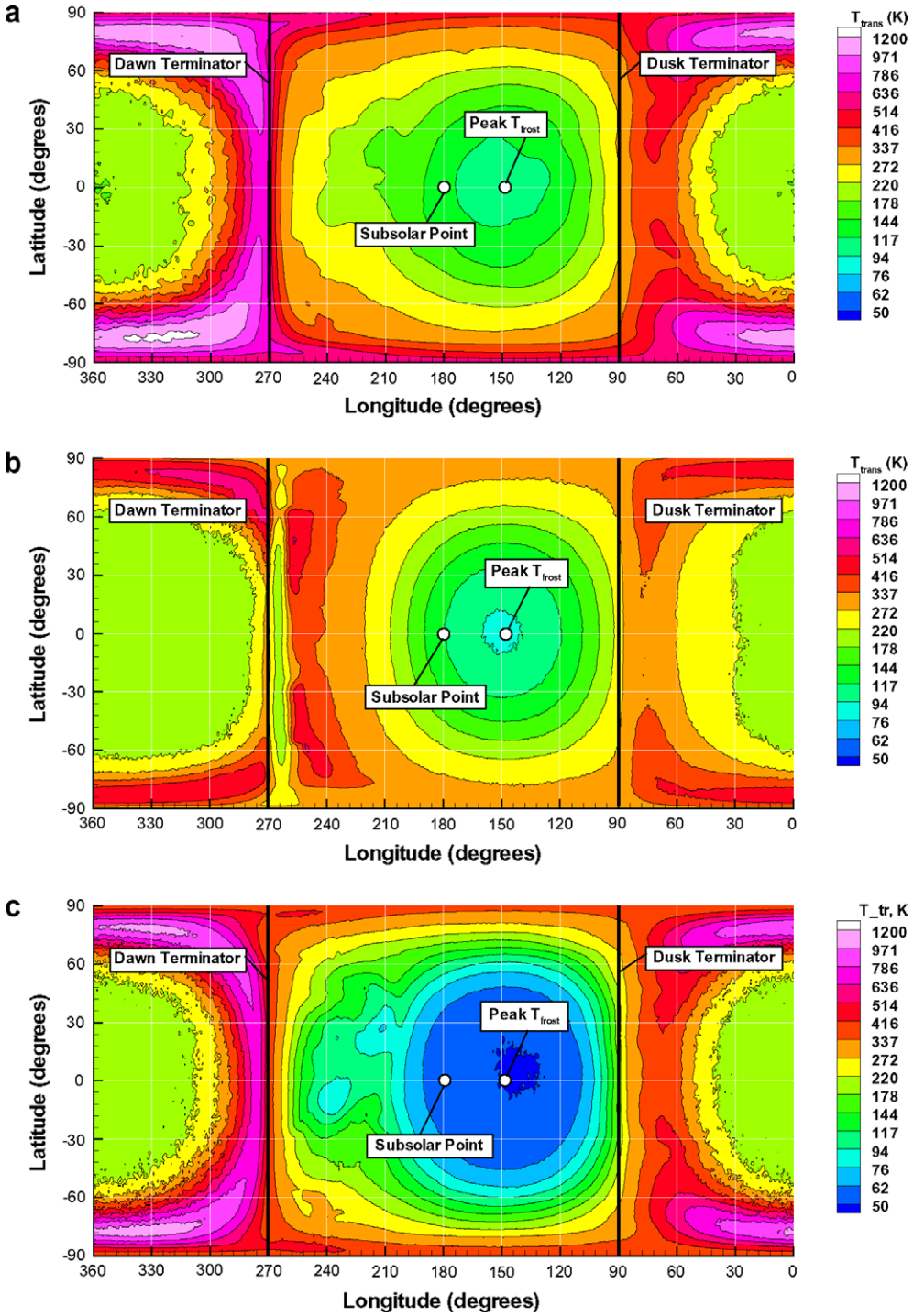

Fig. 11. Color contours of T_{trans} at an altitude of 4 km as a function of latitude and longitude for (a) the baseline atmosphere, (b) Case 2, and (c) Case 3. The dawn and dusk terminators are denoted by the thick black vertical lines. Note the exponential color bar.

T_{rot} is in equilibrium with T_{trans} when the gas density is greater than $\sim 10^9$ cm^{-3}. As the density decreases below this value the collision rate for rotational excitation drops below the threshold needed to sustain equilibrium with T_{trans}. At higher altitudes, T_{trans} continues to increase due to plasma energy input whereas T_{rot} warms more slowly as the energy input from collisions and plasma is not sufficient to balance the energy loss from microwave radiation. For Case 3 (T_{ss} = 120 K), thermal equilibrium is maintained up to ~60 km altitude on the dayside because of the thicker column which raises the altitude of the threshold density (10^9 cm^{-3}) from 40 km to ~60 km; the nightside is unaffected by the change in T_{ss}.

For the baseline atmosphere, the vibrational temperature of the v_2 vibrational mode of SO_2, T_{vib}, is only in equilibrium with T_{trans} very near the surface; everywhere away from the surface T_{vib} is highly non-equilibrium. In Fig. 13a, contours of T_{vib} are shown for the same cross-sectional slice shown in Fig. 9. The nightside is weakly populated at all longitudes and altitudes and there are nearly zero vibrationally excited SO_2 molecules above an altitude

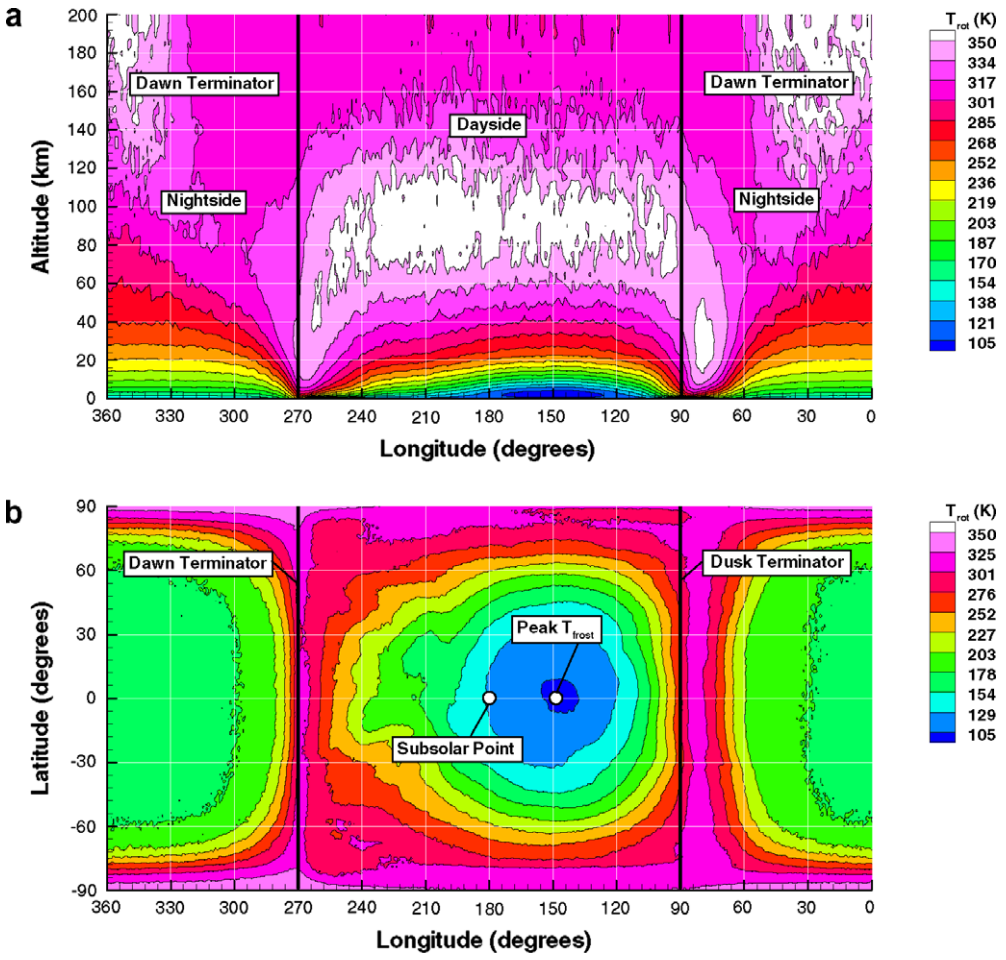

Fig. 12. (a) Contours of T_{rot} for a cross-sectional slice through the baseline atmosphere at the equator. (b) Contours of T_{rot} for a slice through the atmosphere at an altitude of 4 km. Note the different temperature scales for figures (a) and (b).

of 100 km leading to $T_{vib} = 0$. The two mechanisms which can yield a vibrationally excited SO_2 molecule in our current model are collisions and sublimation from the surface (since the departing molecule is assumed to be in thermal equilibrium with the surface). Direct plasma-induced excitation is not modeled. Vibrational de-excitation of an SO_2 molecule occurs rapidly for the ν_2 band which has an Einstein A coefficient of $A_{1\rightarrow0} = 0.88\ s^{-1}$ (Radzig and Smirnov, 1980). A rough estimate of the mean time between collisions can be calculated from:

$$\tau = \frac{\lambda}{\bar{c}} \tag{9}$$

where λ is the mean free path and $\bar{c}$ is the mean velocity of molecules in the gas. For $T_{ss} = 115$ K, the mean time between collisions, τ, is about 0.05 s. Although, the mean time between collisions is shorter than the radiative lifetime of the ν_2 band, not all collisions will vibrationally excite an SO_2 molecule. In fact, relatively few collisions actually excite vibration. The vibrational collision number Z_v is the average number of collisions required before a collision which transfers vibrational energy occurs (Bass et al., 1971). Z_v is a function of temperature and the relative collision energy but it is generally around 300 and never drops below 100 for the conditions present in Io's atmosphere (Zhang et al., 2003). Therefore, it takes ~300 collisions before a molecule undergoes a collision which transfers vibrational energy. Therefore the mean time between vibrational exciting collisions, τ_{vib}, at the location of the peak T_{frost} near the surface is roughly 15 s. Therefore, the vibrational excitation rate by collisions is much slower than the de-excitation rate by radiative emission and this is true everywhere in the atmosphere. In conclusion, near the surface from which the gas sublimates, T_{vib} is in near equilibrium with T_{rot} and T_{trans}, but T_{vib} rapidly becomes non-equilibrium with increasing altitude.

Without another mechanism to populate the ν_2 band, T_{vib} would rapidly asymptote to zero away from the surface. Io's plasma torus supplies such a mechanism. In our model, the plasma heating causes T_{vib} to increase (through collisions with molecules that absorbed plasma energy into their translational and rotational modes) where the atmosphere is sufficiently collisional (dense) and at altitudes above which the plasma has not yet been depleted. When the atmosphere is relatively thick (e.g. near the subsolar point), the plasma energy is completely absorbed by the atmosphere above a certain altitude. For $T_{ss} = 115$ and 120 K, the altitudes at which complete plasma depletion occurs are 2 km and 5 km, respectively. The probability of vibrational energy transfer increases with increasing collision energy. Also, the collision rate increases with T_{trans}. If our current model were altered to allow for direct plasma-induced excitation by depositing an equal amount of energy into vibration, then we would likely see much warmer T_{vib} at high altitudes; however, the ν_2 band radiation emitted from high altitudes would likely remain relatively small due to the low densities.

The latitudinal and longitudinal dependence of T_{vib} can be seen in Fig. 13b which shows a slice of the atmosphere at a constant altitude of 4 km. On the nightside, T_{vib} is too cold to resolve; however,

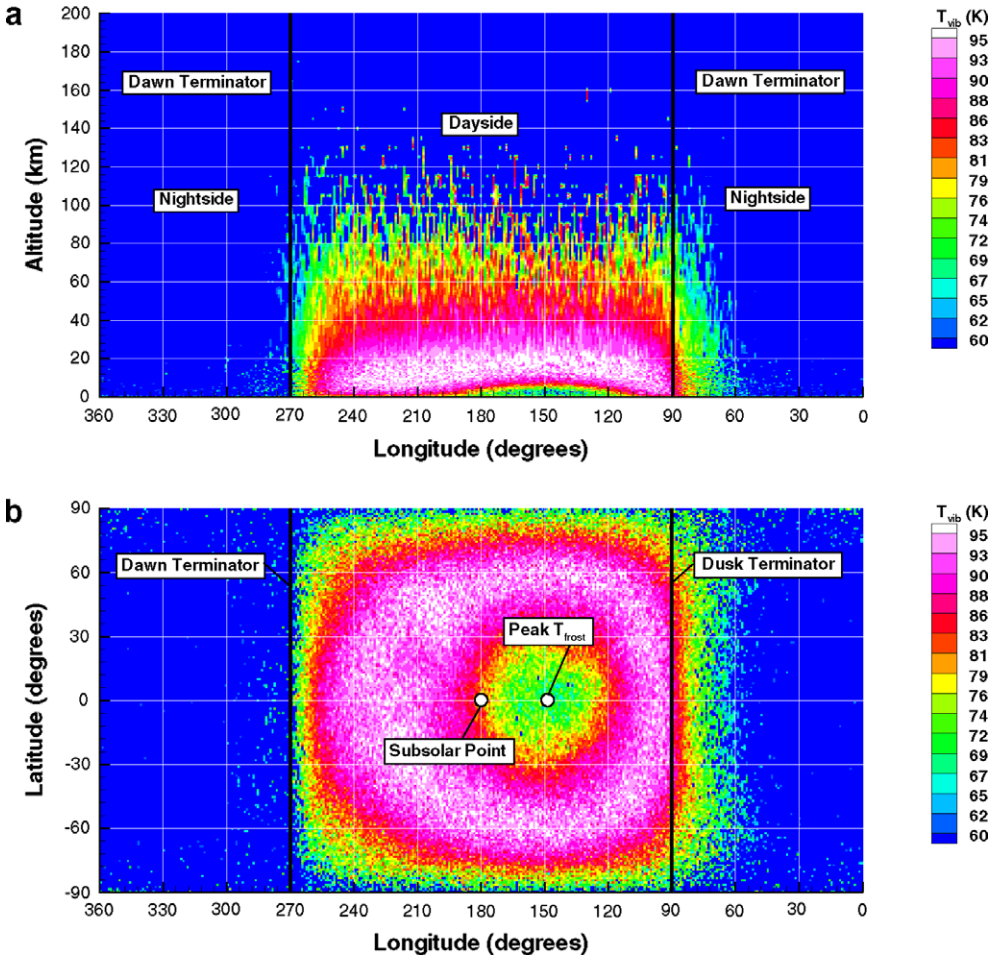

Fig. 13. (a) Color contours of T_{vib} for a cross-sectional slice through the atmosphere at the equator. (b) Color contours of T_{vib} as a function of latitude and longitude at an altitude of 4 km. Results shown are for the baseline atmosphere.

the nightside T_{vib} are unimportant for comparison to observations of the dayside atmosphere (Gratiy et al., 2009).

The T_{vib} contours seen in Fig. 13b exhibit a bullseye pattern on the dayside. T_{vib} is actually colder near the peak T_{frost} because little of the plasma energy reaches this altitude. The "hot" ring of ~95 K T_{vib} corresponds to the region where plasma has penetrated *and* the gas is still sufficiently dense to be collisional. Both the plasma penetration depth and the gas density depend on the T_{frost} which is ~110–112 K in the region below the hot ring. If we look at higher altitudes, then the radius of the bullseye ring will shrink because the gas is not sufficiently dense to have vibrational excitation collisions even with the additional energy from plasma heating. The peak T_{vib} occurs in a "dome" corresponding to areas where the plasma can penetrate and the gas is sufficiently dense (see Fig. 13a). Below this "dome" the gas is colder because the plasma does not penetrate into the gas and collisions (without the input of plasma energy) are rarely energetic enough to excite the vibrational modes. Outside of the "dome", the gas is not sufficiently collisional to transfer translational and rotational energy absorbed from the plasma to the vibrational states. The plasma energy flux can travel through the entire column of gas and strike the surface at longitudes beyond ~40° east and ~100° west of the peak T_{frost}. The difference to the east and west is due to the additional column from the dawn atmospheric enhancement to the west. Likewise, the plasma flux strikes the surface at latitudes beyond ±50°. When T_{ss} = 120 K, the plasma reaches the surface at approximately 55° east and 110° west of the peak T_{frost}. Also, the plasma does not reach the surface until beyond latitudes ±70°. The thicker column at 120 K absorbs more plasma energy allowing the plasma energy flux to reach the surface only on the fringes of the dayside disk. Note that the points at which the plasma can reach the surface would likely change with a more accurate plasma impingement model.

4.3. Number and column densities

The vertical column density is found to be predominantly controlled by the surface temperature (exponential dependence), the molecular residence time of SO_2 on the rocky surface having the second largest effect, the surface frost coverage having a comparatively small effect (proportional), and winds having an even lesser effect. The exponential dependence of the vapor pressure (and hence sublimated flux of SO_2) on T_{frost} explains the overwhelming influence of T_{frost} on the column density (Fig. 14a–c). The increased departures from hydrostatic equilibrium on the morning side of the disk (compared to the evening side) are all due to the dawn atmospheric enhancement. In Fig. 14a–c, the effect of inhomogeneous surface frost on the column density above the surface is evident. The inhomogeneities are seen most strongly on the nightside where the temperature is nearly constant. The column density is larger near regions of high frost fraction and smaller in areas of lit-

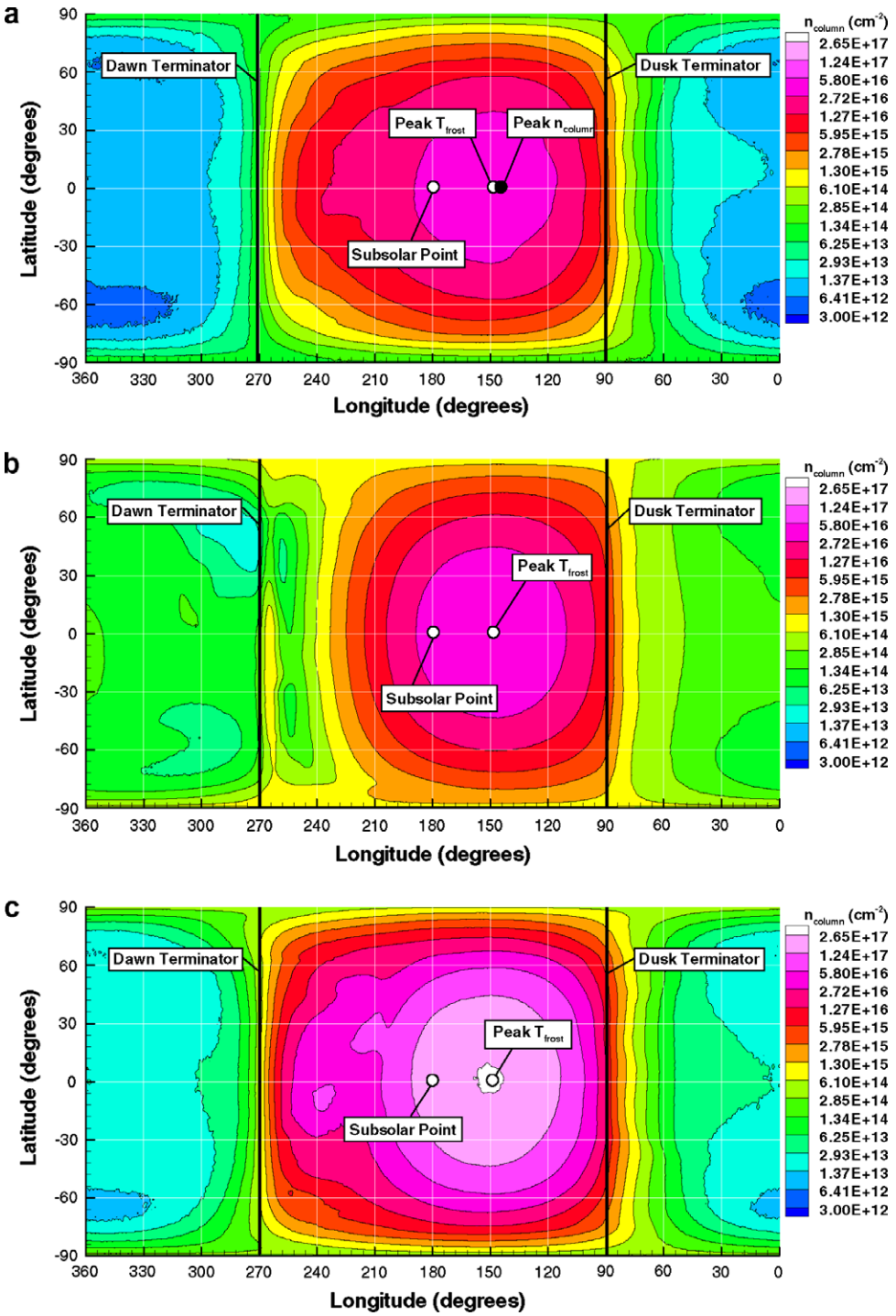

Fig. 14. Color and line contours of the column density as a function of latitude and longitude for (a) the baseline atmosphere, (b) Case 2, and (c) Case 3.

tle frost. Circumplanetary flow is found to negligibly affect the column density for all cases.

For the baseline atmosphere, the *peak* equatorial vertical column density is 4.7×10^{16} cm^{-2} (at 148°W or 2:10 pm) and the subsolar vertical column density is 3.20×10^{16} cm^{-2} (at 180°W or 12:00 pm) with error estimates of $\pm 5 \times 10^{14}$ cm^{-2} on all vertical column densities. The error is based on the noise in cells adjacent to the subsolar and peak equatorial values. The difference between the subsolar and peak vertical column densities is due to the thermal lag discussed in Section 4.1. The morning-side vertical column densities are increased beyond the hydrostatic equilibrium values due to the extended dawn atmospheric enhancement. The nightside vertical column densities at 345°W (1:00 am) vary from 4.5×10^{12} cm^{-2} at 65°S and to 1.3×10^{13} cm^{-2} at the equator due to the latitudinal variation in temperature. The longitudinal variation in nightside vertical column densities is more complicated because of the high surface frost temperatures immediately on the nightside of the dusk terminator. At 85°W (local time ~6:20 pm), the surface frost temperature is ~106 K with a corresponding vertical column density of 1.1×10^{15} cm^{-2}. The various

nightside column densities vary nearly two orders of magnitude due to the high thermal inertia of surface frosts. The vertical column densities inferred from Lyman-α (Feaga et al., 2009) are slightly higher than our sublimation atmosphere. As mentioned in the introduction, Feaga et al. (2009) determined the dayside peak vertical column density to be 5.0×10^{16} cm^{-2} on the anti-jovian hemisphere, 4.2×10^{16} cm^{-2} at the anti-jovian point, and 1.5×10^{16} cm^{-2} at the sub-jovian point. The agreement with our simulations is relatively good and could be improved by increasing our assumed subsolar temperature of the surface to 116 K. It is, however, important to note that the simulated vertical column densities do not include the column from active volcanoes so such an increase in surface temperature may not be needed when the column densities due to volcanoes are included.

For Case 2, the column density is negligibly affected by the surface frost fraction (on the dayside) and is completely controlled by T_{frost} as seen by comparing Fig. 14b with Fig. 3b. In the short residence time model, the mean residence time on the rock surface at 115 K is approximately 5 s (Sandford and Allamandola, 1993). This residence time is short compared to both the ballistic time and the timescale on which the surface temperature varies. Also, the mean frost fraction at any given longitude never increases beyond 0.60 (see Fig. 8). Molecules which hit the surface will therefore have a 40% or greater chance of hitting a rock surface and being promptly desorbed. In areas where the frost fraction is even lower, the likelihood of molecules desorbing from the surface increases and therefore these areas will be more populated by molecules that have collided with the surface. Therefore, molecules which hit the rock surface are able to flow/diffuse over long distances to regions of lower pressure and laterally equilibrate the pressure such that it is only based on the T_{frost}. This type of far reaching pressure control for hot and dry (non-frost/rock) surfaces was discussed by Ingersoll (1989). The column density increases everywhere on the dayside because of the rapid rate at which molecules escape from the warm rock surface into the atmosphere when the residence time is short. For Case 2, the peak equatorial column density is 5.45×10^{16} cm^{-2} (at 148°W or 2:10 pm) and the subsolar vertical column density is 3.7×10^{16} cm^{-2} (at 180°W or 12:00 pm) The Case 2 column densities are ~10% higher than the baseline atmosphere. The vertical column density also departs from hydrostatic equilibrium for Case 2 at the location of the dawn atmospheric enhancement (Fig. 14b). At this location, the atmosphere is not sustained by sublimation from the frost, but instead by the rapid desorption of all the SO_2 gas which condensed onto rock during the night.

For Case 3, the peak equatorial vertical column density is 2.73×10^{17} cm^{-2} and the subsolar vertical column density is 1.85×10^{17} cm^{-2}. These T_{ss} = 120 K column densities are 5 times as large as the T_{ss} = 115 K values and are above the upper range of observed column densities (1.25×10^{17} cm^{-2} – Jessup et al., 2004; 1.5×10^{17} cm^{-2} – Spencer et al., 2005). The T_{ss} = 120 K values are thus an upper limit on the vertical column densities and associated flow strengths.

When the baseline atmosphere has volcanoes superimposed, the column density near "persistent" volcanoes increases dramatically while the subsolar vertical column density remains the same as there are no "persistent" volcanoes close to the subsolar point for the baseline atmosphere's subsolar longitude of 180°W. The peak equatorial value however increases to 1.0×10^{17} cm^{-2} because of the additional column from Prometheus. The peak dayside vertical column density increases to $\sim 7 \times 10^{17}$ cm^{-2} near the center of Prometheus (at 140°W).

Plasma heating is found to alter the vertical density profile of the atmosphere but not change the vertical column density. The vertical column remains unchanged despite the plasma heating because it is sustained by the vapor pressure at the surface which is dependent only on T_{frost}. Plasma heating inflates the atmosphere everywhere on the planet for all cases (see Fig. 15).

Besides comparing the magnitude of the vertical column densities at specific locations, the overall morphology can be compared (see Fig. 16a). A striking feature of the Lyman-α inferred column densities is the sharp fall off in column near ±45° latitude (Strobel and Wolven, 2001; Feaga et al., 2009). The latitudinal variation in our modeled column densities exhibits a much smaller decrease at mid-latitudes than those inferred from the Lyman-α observations. The column density variation in our model is directly related to T_{frost} which at the peak T_{frost} essentially follows a $\cos^{1/4}(\psi)$ latitudinal variation. There are several possible explanations for the differences between the Lyman-α results and our model column densities. These include: (i) unobserved (and un-modeled) latitudinal variations in the T_{frost} distribution, (ii) volcanic plumes located primarily at low latitudes, or (iii) ion-etched surface frosts near the poles.

To examine the first possibility, the average global dayside atmospheric column compiled by Feaga et al. (2009) is used to infer the required latitudinal variation in T_{frost} to support the column. Feaga et al.'s global dayside map averages several instantaneous maps at different subsolar longitudes and as a result the longitudinal variation in the column is dependent only on the frost fraction and volcanic plumes. The global dayside map still retains informa-

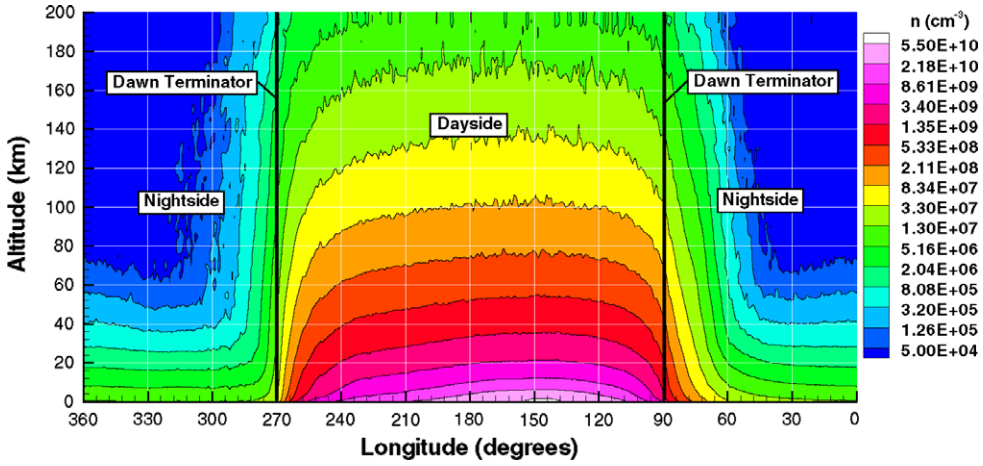

Fig. 15. Color and line contours of the number density for a cross-sectional slice through the atmosphere at the equator for the baseline case. (For interpretation of the references to color in this figure legend, the reader is referred to the web version of this article.)

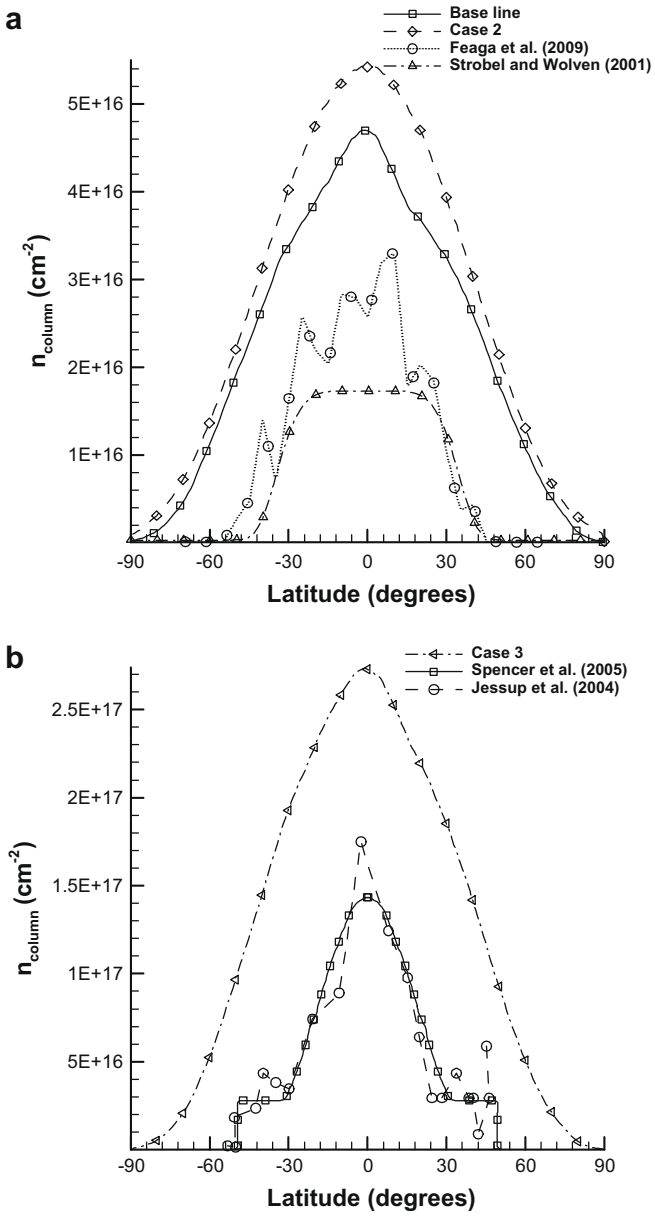

Fig. 16. (a) The latitudinal variation in column density for our simulated baseline atmosphere, Case 2 (both at 148°W), Strobel and Wolven's empirical model (2001), and data extracted at 150°W from Feaga et al.'s (2009) global dayside atmosphere. (b) The latitudinal variation in column density for Case 3 (at 148°W), Jessup et al. (2004) at 153°W, and Spencer et al. (2005) at 180°W.

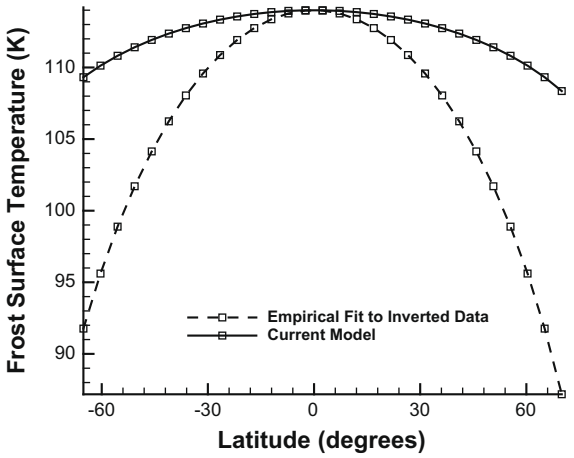

Fig. 17. A comparison of the latitudinal temperature variation derived from Lyman-α inferred columns with our current model's latitudinal temperature variation. Our current model has a $\cos^{1/4}(\psi)$ latitudinal variation at the longitude of the peak T_{frost}.

tion on the latitudinal variation of the atmospheric column. Based on the results stated earlier in this section, the column densities are not significantly affected by the circumplanetary winds. Therefore, we assume that an analytic atmosphere in hydrostatic equilibrium based only on T_{frost} and the frost fraction is a fairly accurate approximation (especially away from the morning side where the dawn atmospheric enhancement affects the atmosphere). With this analytic representation for the column density, the global dayside atmosphere based on Lyman-α (obtained from Feaga et al. (2009)) can be inverted to find the required latitudinal variation in T_{frost} (as seen in Fig. 17). The observed Lyman-α column variation requires T_{frost} to drop much faster than predicted by a $\cos^{1/4}(\psi)$ law. At ±45° latitude, the temperature inferred from Lyman-α observations (Feaga et al., 2009) is ~104 K which is ~8 K colder than our current model. However, such a sharp drop in the surface temperature is difficult to distinguish from the thermal anomalies in the Galileo PPR observations (Rathbun et al., 2004).

The second possibility is that the column is primarily supported by volcanic activity. Many of the large "persistent" volcanoes on Io are clustered in a band within ±30° of the equator (Geissler et al., 2004) which does correlate with the equatorial "belt" atmosphere seen in the Lyman-α observations. The arguments both for and against volcanoes being the primary constituent of the atmosphere are presented by Spencer et al. (2005). Among the arguments against, the instantaneous column density maps (Feaga et al., 2009) are surprisingly smooth whereas a volcanically supported atmosphere should be regional and patchy (as seen in Fig. 4). Also, the instantaneous maps showed little temporal variation while several of the large volcanoes are known to have had temporal variations during the observational period (Feaga et al., 2009).

The third possibility is that the plasma is impacting the surface at latitudes beyond ±45°. The plasma ions and neutrals could alter the composition of the surface frost and reduce the sublimation atmosphere near the poles.

Another major feature of the Lyman-α inferred column densities is the anti-jovian/sub-jovian hemisphere asymmetry, where the anti-jovian hemisphere exhibits higher column densities than the sub-jovian hemisphere. To compare with the Lyman-α observations, the column densities at six subsolar longitudes (each the product of a full numerical simulation) are averaged along different geometries and compared (see Fig. 18). The column densities peak at the anti-jovian point (180°W) and 240°W and show the expected overall trend with the anti-jovian hemisphere having higher averaged column than the sub-jovian hemisphere. The anti-jovian/sub-jovian column density asymmetry in Fig. 18 is caused solely by the surface frost fraction (Douté et al., 2001). Note that eclipse of the sub-jovian hemisphere is not modeled.

The Lyman-α inferred dayside column densities (at a given subsolar longitude) are also nearly constant with local time of day which does not match our current sublimation atmosphere model. The possible reasons for the discrepancy are that the surface frosts have an even higher thermal inertia than modeled here and therefore the surface frosts have nearly uniform surface temperature throughout the day. Another explanation is that the atmosphere is not supported by sublimation but instead by equatorial-biased volcanic plumes.

In Fig. 16b, the latitudinal variation of the vertical column density of Case 3 is compared to the upper range of recent observations (Jessup et al., 2004; Spencer et al., 2005). Case 3 is much

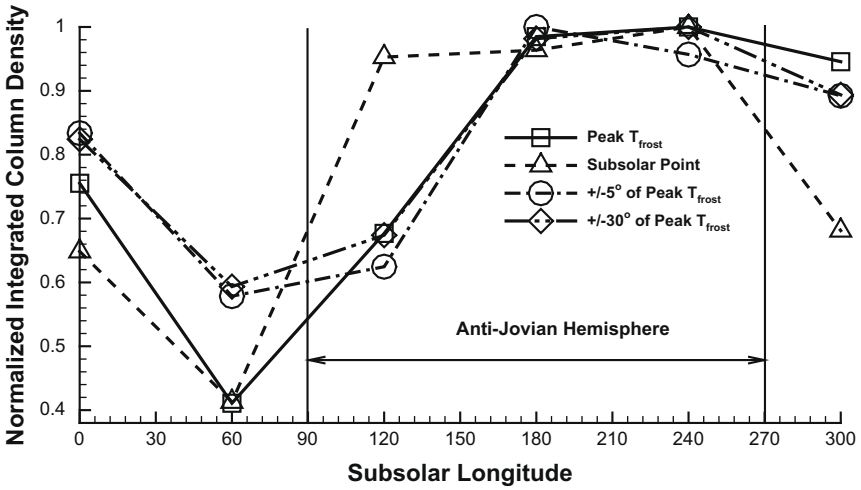

Fig. 18. The integrated column density (normalized by the maximum value) for subsolar longitudes of 0°, 60°, 120°, 180°, 240°, and 300°. Each subsolar longitude has the column density integrated along the following paths or areas: the longitude of peak T_{frost} from the north to south pole, the subsolar longitude from the north to south pole, in a 5° by 5° region around the point of peak T_{frost}, and in a 30° by 30° region around the point of peak T_{frost}. All integration areas show roughly the same trend. Eclipse of the sub-jovian hemisphere is not considered.

higher than either observational data set at all latitudes. The upper range data sets can also be compared with the baseline and Case 2 atmospheres (although they are not plotted together). Both Jessup et al. (2004) and Spencer et al. (2005) predict much higher column densities (2–3 times larger) than the baseline or Case 2 atmospheres.

A detailed comparison of our atmospheric model to the observations in the mid-IR, Lyman-α, and millimeter ranges is presented in a companion paper (Gratiy et al., 2009). That paper applies a new three-dimensional spherical-shell radiative transfer code utilizing a photon backward Monte Carlo method to simulate spectra and images from the atmosphere, which can then be directly compared to observations. Such analysis provides important feedback for improvement of the physical parameters which govern the atmospheric model's dynamics. A brief summary of the results found in our companion paper is given next.

Gratiy et al. find that our baseline sublimation atmosphere with volcanic plumes superimposed is the best fit to the longitudinal asymmetries found in the infrared observations of Spencer et al. (2005). Band depths derived from our model atmosphere show the anti-jovian hemisphere has a higher band depth than the sub-jovian hemisphere; however, the band depths derived from our model are slightly higher between 240° and 360° than Spencer et al. (2005). Our Case 2 atmosphere is found to have negligible change in band depth as the longitude varies, while the Case 2 composite atmosphere (with volcanic plumes superimposed) is still a poor match. Both Case 2 atmospheres are poor fits because the short residence time smoothes any inhomogeneities created by the surface frost map. Case 3 was not investigated.

Comparison to the Lyman-α observations (Feaga et al., 2009) by Gratiy et al. shows that our baseline and Case 2 atmospheres match the peak observed intensity but the overall morphology disagrees with the observations for all atmospheric cases. Our model does not agree with the latitudinal or longitudinal variation in Lyman-α intensity as discussed earlier. Possible reasons for the discrepancy are discussed in Gratiy et al. (2009).

Disk-resolved millimeter observations (Moullet et al., 2008) can yield important information on variation of winds around Io. Gratiy et al. simulated the millimeter line profiles that would be observed based on our baseline sublimation and composite atmospheres and found that the atmospheric dynamics (circumplanetary winds and plumes) favorably explain the observed line widths, whereas the line widths are too narrow when only the thermal Doppler effect contributes to broadening. Gratiy et al. also found a similar limb-to-limb velocity difference which agrees well with millimeter observations; however, these observations show a blue shift on the eastern limb which is not predicted by our model.

5. Conclusions

We have used the DSMC method to simulate the rarefied gas dynamics on Io. These simulations have improved on the previous work on circumplanetary flow by Austin and Goldstein (2000) by including inhomogeneous frost coverage, three-dimensionality, and a rotating temperature distribution which includes the effects of thermal inertia. Our model also properly accounts for the rarefied conditions present in much of Io's atmosphere unlike the previous continuum models (Ingersoll et al., 1985; Moreno et al., 1991; Wong and Johnson, 1995; Wong and Smyth, 2000; Smyth and Wong, 2004). Many of our results are in agreement with earlier work, but we have also attempted to reconcile our findings with observations of: surface temperature (Rathbun et al., 2004), frost fraction (Douté et al., 2001), column density of the atmosphere (Feaga et al., 2009), and mid-IR observations of the ν_2 vibrational band of SO_2 (Spencer et al., 2005).

We find that the pressure gradient from the warm dayside to the cold nightside is strong enough to drive the flow supersonic with both T_{ss} = 115 K and 120 K and with a nightside temperature of 90 K. The flow diverges in all directions away from the region of peak T_{frost} and forms a region of supersonic flow near the terminator for all cases. The influence of the residence time was investigated by comparing a short residence time model that treats the rock surface as being coated by a thin layer of SO_2 (Sandford and Allamandola, 1993) to a longer residence time model. The short residence model creates a rapid outflux of SO_2 molecules at the dawn terminator that we refer to as the dawn atmospheric enhancement. The longer residence time model simulates slower effective desorption rates due to the possibility of multiple bounces within a very porous surface (Matson and Nash, 1983). This model is preferred because it better matches the longitudinal asymmetries in band depth detected in mid-IR observations (Spencer et al., 2005; Gratiy et al., 2009). The magnitude of the Mach number around the terminator varies due to the asymmetric surface temperature distribution for the short residence time model

and the dawn atmospheric enhancement. The long residence time model exhibits further variations due to the inhomogeneous surface frost. The rotating temperature distribution had significant effects on the structure of the atmosphere. The peak T_{frost} lags the subsolar point by ~32° because of the modeled high thermal inertia of the frost. Therefore, the column density generally lagged the subsolar point by the same amount with minor differences due to the frost map. Such a large lag in T_{frost} is not observed in Lyman-α (Feaga et al., 2009) nor in IR observations (Rathbun et al., 2004), but the high thermal inertia in our model is required to match the nightside cooling rate of the brightness temperature observed by Rathbun et al. (2004). We are currently transitioning to a more accurate temperature distribution that models the conduction into the surface which may allow high thermal inertias without creating such a large lag between the peak T_{frost} and the subsolar point.

By altering the amount of sublimation from the surface based on a non-uniform frost map (Douté et al., 2001) and using a temperature distribution similar to observations (Rathbun et al., 2004), we achieved good agreement with the magnitudes of the column densities observed in the Lyman-α (Feaga et al., 2009). We were, however, unable to reconcile the latitudinal column density morphology inferred from the Lyman-α observations (Feaga et al., 2009). The steep drop in the inferred column near ±45° latitude from Lyman-α observations remains unresolved but could be due to several phenomena discussed in Section 4.3.

Acknowledgments

This research was supported the NASA Planetary Atmospheres Grant NNG05G083G and Outer Planets Research Grant NNX08AQ49G. Computations were performed at the Texas Advanced Computing Center.

References

Austin, J.V., Goldstein, D.B., 2000. Rarefied gas model of Io's sublimation-driven atmosphere. Icarus 148, 370–383.
Ballester, G.E., Strobel, D.F., Moos, H.W., Feldman, P.D., 1990. The atmospheric abundance of SO_2 on Io. Icarus 88, 1–23.
Ballester, G.E., McGrath, M.A., Strobel, D.F., Zhu, X., Feldman, P.D., Moos, H.W., 1994. Detection of the SO_2 atmosphere on Io with the Hubble Space Telescope. Icarus 111, 2–17.
Bass, H.F., Winter, T.G., Evans, L.B., 1971. Vibrational and rotational relaxation in sulfur dioxide. J. Chem. Phys. 54, 644–647.
Binder, A.B., Cruikshank, D.P., 1964. Evidence for an atmosphere on Io. Icarus 3, 299–305.
Bird, G.A., 1994. Molecular Gas Dynamics and the Direct Simulation of Gas Flows. Oxford Univ. Press, Oxford.
Carlson, R.W., and 10 colleagues, 1997. The distribution of sulfur dioxide and other infrared absorbers on the surface of Io. Geophys. Res. Lett. 24, 2479–2482.
Clarke, J.T., Ajello, J., Luhmann, J., Schneider, N., Kanik, I., 1994. Hubble Space Telescope UV spectral observations of Io passing into eclipse. J. Geophys. Res. 99, 8387–8402.
Cruikshank, D.P., Murphy, R.E., 1973. The post-eclipse brightening of Io. Icarus 20, 7–17.
Douté, S., Schmitt, B., Lopes-Gautier, R., Carlson, R., Soderblom, L., Shirley, J., and the Galileo NIMS Team, 2001. Mapping SO_2 frost on Io by the modeling of NIMS hyperspectral images. Icarus 149, 107–132.
Feaga, L.M., 2005. Hubble Space Telescope Far-Ultraviolet Observations of Io: Determining Atmospheric Abundances, Mapping the SO_2 Distribution, and Correlating the Molecular and Atomic Atmosphere. PhD Dissertation, Johns Hopkins University.
Feaga, L.M., McGrath, M., Feldman, P.D., 2009. Io's dayside SO_2 atmosphere. Icarus 201, 570–584.
Feldman, P.D., Strobel, D.F., Moos, H.W., Retherford, K.D., Wolven, B.C., McGrath, M.A., Roesler, F.L., Woodward, R.C., Oliverson, R.J., Ballester, G.L., 2000. Lyman-α imaging of the SO_2 distribution on Io. Geophys. Res. Lett. 27, 1787–1790.
Frank, L.A., Paterson, W.R., Ackerson, K.L., Vasyliunas, W.M., Corniti, F.V., Bolton, S.J., 1996. Plasma observations at Io with the Galileo spacecraft. Science 274, 394–395.
Franz, O.G., Millis, R.L., 1971. A search for an anomalous brightening of Io after eclipse. Icarus 14, 13–15.
Geissler, P.E., McEwen, A.S., Keszthelyi, L., Lopes-Gautier, R., Granahan, J., Simonelli, D.P., 1999. Global color variations on Io. Icarus 140, 265–282.
Geissler, P., McEwen, A., Philips, C., Keszthelyi, L., Spencer, J., 2004. Surface changes on Io during the Galileo mission. Icarus 169, 29–64.
Gratiy, S.L., Walker, A.C., Levin, D.A., Goldstein, D.B., Varghese, P.L., Trafton, L.M., Moore, C.M., 2010. Multi-wavelength simulations of atmospheric radiation from Io with a 3-D spherical-shell backward Monte Carlo radiative transfer model. Icarus 207 (1), 394–408.
Hendrix, A.R., Barth, C.A., Hord, C.W., 1999. Io's patchy SO_2 atmosphere as measured by the Galileo ultraviolet spectrometer. J. Geophys. Res. 104, 11817–11826.
Howell, R.R., Cruikshank, D.P., Fanale, F.P., 1984. Sulfur dioxide on Io: Spatial distribution and physical state. Icarus 57, 83–92.
Ingersoll, A.P., 1989. Io meteorology: How atmospheric pressure is controlled locally by volcanos and surface frosts. Icarus 81, 298–313.
Ingersoll, A.P., Summers, M.E., Schlipf, S.G., 1985. Supersonic meteorology of Io: Sublimation-driven flow of SO_2. Icarus 64, 375–390.
Jessup, K.L., Ballester, G.E., Combi, M., Zhu, X., Strobel, D.F., Clarke, J.T., 2002. Io's changing atmosphere. In: The Magnetospheres of the Outer Planets Conference Abstract Book, p. 116.
Jessup, K.L., Spencer, J.R., Ballester, G.E., Howell, R.R., Roesler, F., Vigel, M., Yelle, R., 2004. The atmospheric signature of Io's Prometheus plume and anti-jovian hemisphere: Evidence for a sublimation atmosphere. Icarus 169, 197–215.
Kerton, C.R., Fanale, F.P., Salvail, J.R., 1996. The state of SO_2 on Io's surface. J. Geophys. Res. 101, 7555–7563.
Kliore, A.J., Fjeldbo, G., Seidel, B.L., Sweetnam, D.N., Sesplaukis, T.T., Woiceshyn, P.M., 1975. The atmosphere of Io from Pioneer 10 radio occultation measurements. Icarus 24, 407–410.
Laver, C., de Pater, I., 2008. Spatially resolved SO_2 ice on Io, observed in the near IR. Icarus 195, 752–757.
Laver, C., de Pater, I., 2009. The global distribution of sulfur dioxide ice on Io, observed with OSIRIS with the W.M. Keck telescope. Icarus 201, 172–181.
Lellouch, E., 1996a. Detection of sulfur monoxide in Io's atmosphere. Astrophys. J. 459, 107–110.
Lellouch, E., 1996b. Io's atmosphere: Not yet understood. Icarus 124, 1–21.
Lellouch, E., Belton, M., de Pater, I., Gulkis, S., Encrenaz, T., 1990. Io's atmosphere from microwave detection of SO_2. Nature 369, 639–641.
Lellouch, E., Belton, M., de Pater, I., Paubert, G., Gulkis, S., Encrenaz, T., 1992. The structure, stability, and global distribution of Io's atmosphere. Icarus 98, 271–295.
Linker, J.A., Kivelson, M.G., Walker, R.J., 1988. An MHD simulation of plasma flow past Io: Alfven and slow mode perturbations. Geophys. Res. Lett. 15, 1311–1314.
Marchis, F., and 11 colleagues, 2005. Keck AO survey of Io global volcanic activity between 2 and 5 μm. Icarus 176, 96–122.
Matson, D.L., Nash, D.B., 1983. Io's atmosphere: Pressure control by regolith cold trapping and surface venting. J. Geophys. Res. 88, 4471–4783.
McEwen, A.S., Johnson, T.V., Matson, D.L., Soderblom, L.A., 1988. The global distribution, abundance, and stability of SO_2 on Io. Icarus 75, 450–478.
McGrath, M.A., Belton, M.J.S., Spencer, J.R., Sartoretti, P., 2000. Spatially resolved spectroscopy of Io's Pele plume and SO_2 atmosphere. Icarus 146, 476–493.
Moore, C.H., Goldstein, D.B., Varghese, P.L., Trafton, L.M., Stewart, B., 2009. 1-D DSMC simulation of Io's atmospheric collapse and reformation during and after eclipse. Icarus 201, 585–597.
Moreno, M.A., Schubert, G., Baumgardner, J., Kivelson, M.G., Paige, D.A., 1991. Io's volcanic and sublimation atmospheres. Icarus 93, 63–81.
Moullet, A., Lellouch, E., Moreno, R., Gurwell, M.A., Moore, C., 2008. First disk-resolved millimeter observations of Io's surface and atmosphere. Astron. Astrophys. 482, 279–292.
Nash, D.B., Fanale, F.P., Nelson, R.M., 1980. SO_2 frost: UV–visible reflectivity and Io surface coverage. Geophys. Res. Lett. 7, 64–67.
Nelson, R.M., Lane, A., Matson, D., Fanale, F., Nash, D., Johnson, T., 1980. Io's longitudinal distribution of sulfur dioxide frost. Science 210, 784–786.
O'Leary, B., Veverka, J., 1971. On the anomalous brightening of Io after eclipse. Icarus 14, 265–268.
Pearl, J., Hanel, R., Kunde, V., Maguire, W., Fox, K., Gupta, S., Ponnamperuma, C., Raulin, F., 1979. Identification of gaseous SO_2 and new upper limits for other gases on Io. Nature 280, 755–758.
Pospieszalska, M.K., Johnson, R.E., 1996. Monte Carlo calculations of plasma ion-induced sputtering of an atmosphere: SO_2 ejected from Io. J. Geophys. Res. 101, 7565–7573.
Radzig, A.A., Smirnov, B.M., 1980. Reference Data on Atoms, Molecules, and Ions. Springer-Verlag.
Rathbun, J.A., Spencer, J.R., Davies, A.G., Howell, R.R., Wilson, L. 2002. Loki, Io: A periodic volcano. Geophys. Res. Lett. 29. doi:10.1029/2002GL014747.
Rathbun, J.A., Spencer, J.R., Tamppari, L.K., Martin, T.Z., Barnard, L., Travis, L.D., 2004. Mapping of Io's thermal radiation by the Galileo photopolarimeter–radiometer (PPR) instrument. Icarus 169, 127–139.
Roesler, F.L., Moos, H.W., Oliversen, R.J., Woodward Jr., R.C., Retherford, K.D., Scherb, F., McGrath, M.A., Smyth, W.H., Feldman, P.D., Strobel, D.F., 1999. Far-ultraviolet imaging spectroscopy of Io's atmosphere with HST/STIS. Science 283, 353–357.
Sandford, S.A., Allamandola, L.J., 1993. The condensation and vaporization behavior of ices containing, SO_2, H_2S, and CO_2: Implications for Io. Icarus 106, 478–488.
Sartoretti, P., McGrath, M.A., Paresce, F., 1994. Disk-resolved imaging of Io with the Hubble Space Telescope. Icarus 108, 272–284.
Saur, J., Strobel, D.F., 2004. Relative contributions of sublimation and volcanoes to Io's atmosphere inferred from its plasma interaction during solar eclipse. Icarus 171, 411–420.

Sinton, W.M., Kaminski, C., 1988. Infrared observations of eclipses of Io, its thermophysical parameters, and the thermal radiation of the Loki volcano and environs. Icarus 75, 207–232.

Sinton, W.M., Tokunaga, A.T., Becklin, E.E., Gatley, I., Lee, T.J., Lonsdale, C.J., 1980. Io: Ground-based observations of hot spots. Science 210, 1015–1017.

Smyth, W.H., Wong, M.C., 2004. Impact of electron chemistry on the structure and composition of Io's atmosphere. Icarus 171, 171–182.

Spencer, J.R., Rathbun, J.A., Travis, L.D., Tamppari, L.K., Barnard, L., Martin, T.Z., McEwen, A.S., 2000. Io's thermal emission from the Galileo photopolarimeter–radiometer. Science 288, 1198–1201.

Spencer, J.R., Lellouch, E., Richter, M.J., López-Valverde, M.A., Jessup, K.L., Greathouse, T.K., Flaud, J., 2005. Mid-infrared detection of large longitudinal asymmetries in Io's SO_2 atmosphere. Icarus 176, 283–304.

Stewart, B.D., Pierazzo, E., Goldstein, D.B., Varghese, P.L., Trafton, L.M., Moore, C.H., 2009. Parallel 3D hybrid continuum/DSMC method for unsteady expansions into a vacuum. AIAA Paper 2009-266. In: 47th AIAA Aerospace Science Meeting, Orlando, FL.

Strobel, D.F., Wolven, B.C., 2001. The atmosphere of Io: Abundances and sources of sulfur dioxide and atomic hydrogen. Astrophys. Space Sci. 277, 271–287.

Strobel, D.F., Zhu, X., Summers, M.E., 1994. On the vertical structure of Io's atmosphere. Icarus 111, 18–30.

Trafton, L.M., Caldwell, J.J., Barnet, C., Cunningham, C.C., 1996. The gaseous sulfur dioxide abundance over Io's leading and trailing hemispheres: HST spectra of Io's C^1B_2–X^1A_1 band of SO_2 near 2100 Å. Astrophys. J. 456, 384–392.

Veeder, G.J., Matson, D.L., Johnson, T.V., Blaney, D.L., Goguen, J.D., 1994. Io's heat flow from infrared radiometry: 1983–1993. J. Geophys. Res. 99, 17095–17162.

Wagman, D., 1979. Sublimation Pressure and the Enthalpy of SO_2. Chem. Thermodyn. Data Cent., Natl. Bur. of Stand.

Wong, M.C., Johnson, R.E., 1995. The effect of plasma heating on sublimation-driven flow in Io's atmosphere. Icarus 115, 109–118.

Wong, M.C., Johnson, R.E., 1996. A three-dimensional azimuthally symmetric model atmosphere for Io 1, photochemistry and the accumulation of a nightside atmosphere. J. Geophys. Res. 101, 23243–23254.

Wong, M.C., Smyth, W.H., 2000. Model calculations for Io's atmosphere at eastern and western elongations. Icarus 146, 60–74.

Zhang, J., Goldstein, D.B., Varghese, P.L., Gimelshein, N.E., Gimelshein, S.F., Levin, D.A., 2003. Simulation of gas dynamics and radiation in volcanic plumes on Io. Icarus 163, 182–197.

Zhang, J., Goldstein, D.B., Varghese, P.L., Trafton, L., Moore, C., Miki, K., 2004. Numerical modeling of ionian volcanic plumes with entrained particulates. Icarus 172, 479–502.